8-15-2018

A Mathematical Model of Fluid Flow in Evaporating Droplets Using Wedge Geometry

Jordana O'Brien
jeo8857@rit.edu

A Mathematical Model of Fluid Flow in Evaporating Droplets Using Wedge Geometry

by

Jordana O'Brien

A Thesis Submitted in Partial Fulfillment of the Requirements
for the Degree of Master of Science in Applied Mathematics
School of Mathematical Sciences, College of Science

Rochester Institute of Technology
Rochester, NY
August 15, 2018

Committee Approval:

R·I·T
College of
SCIENCE

Kara Maki, Ph.D. Date

School of Mathematical Sciences

Thesis Advisor

Michael Schertzer, Ph.D. Date

Kate Gleason College of Engineering

Committee Member

Steven Weinstein, Ph.D. Date

Kate Gleason College of Engineering

Committee Member

Nathaniel Barlow, Ph.D. Date

School of Mathematical Sciences

Committee Member

Matthew Hoffman, Ph.D. Date

School of Mathematical Sciences

Director of Graduate Programs

Abstract

As a droplet of liquid evaporates, particles within the droplet are often pulled to the edge and deposited in a ring-shaped pattern. This is known as the coffee-ring effect. The coffee-ring effect is largely due to evaporation taking place at a pinned contact line. Since this formation is an adverse outcome in many practical applications, methods to counteract the coffee-ring effect have become of interest, including the application of an electric field. In this research project, we discuss the first stage in constructing a coupled mathematical model of colloidal transport within an evaporating droplet under the influence of an electric field. The first stage is to simply capture the fluid flow within a pinned evaporating droplet without any consideration of particles or an electric field. We consider a thin axisymmetric droplet of a Newtonian solvent in contact with ambient air that is undergoing diffusion-limited evaporation. Away from the contact line, we model the droplet dynamics by applying the lubrication approximation to simplify the Navier-Stokes equations. To characterize the flow near the contact line, we assume the droplet shape is a wedge and derive analytical solutions of evaporative-driven Stokes flow near a pinned contact line. We connect the lubrication model and the wedge model by specifying height and flux conditions at the boundary between the two regions. We solve for the position of the droplet interface by implementing a method of lines approach in MATLAB. We find that for our specified conditions, the two regions evaporate on different time scales. However, if either the evaporation rate or the rate of contact angle decrease is appropriately adjusted, the two regions evaporate simultaneously.

Contents

I. Introduction

I.1 Motivation

Evaporation of colloidal droplets is a mechanism widely used for a variety of purposes. In this process, microscopic, insoluable particles (between 1 nanometer and 1 micron) are dispersed throughout a liquid medium deposited on a substrate. As a colloidal droplet evaporates, particles are transported throughout the droplet by fluid motion and eventually stick to the substrate as fluid is lost. The residual formation left behind by a completely evaporated droplet is known as the deposition pattern. Particle deposition affects a variety of applications from inkjet printing [3, 10, 25, 29, 30] to medical diagnostics [2, 11]. In the classic coffee-ring effect, particles are deposited at the periphery of the droplet, leaving behind a dark ring. This is due to increased evaporation taking place at a pinned contact line [8, 9]. Mass conservation requires that fluid removed by evaporation from the contact line region be replenished by fluid from the center of the drop. This drives an outward radial flow which pulls particles toward the pinned periphery. The non-homogeneous pattern observed in the coffee-ring effect can be leveraged in certain contexts. One such context is in the manufacturing of flexible electronic devices in which conductive material is inkjet printed onto a flexible surface to create circuitry [3, 29, 30]. However, other applications rely on uniform deposition patterns [10, 11, 25]. Hence, it would be advantageous to have a method by which the desired deposition pattern can consistently be obtained. To this end, various strategies have been proposed to suppress the coffee-ring effect. Some successful strategies for coffee-ring suppression include the addition of surfactants, which involve surface tension gradients that counteract the outward radial flow towards the contact line [16]; deformation of the interface by use of non-spherical colloids [31]; and the application of an electric field [5, 12, 24, 19], which has the potential to disrupt the dynamics of particle motion near the contact line by introducing an electrowetting force at the contact line and an electrophoretic force on charged colloids in a droplet.

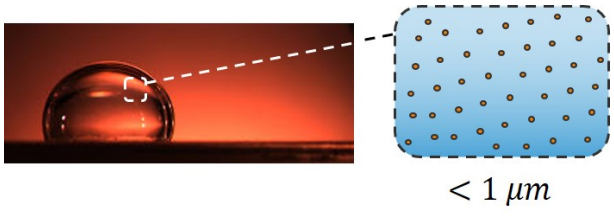

Figure 1: Image of a colloidal droplet. Particle diameter ranges from 1 nanometer to 1 micron.

In collaboration with the Discrete Micro-Fluidics Laboratory (DMFL) at the Rochester Institute of Technology (RIT), we seek to develop a device that utilizes both ring-like and uniform deposition patterns to detect the presence and concentration of target proteins. In our proposed method, an electric field is applied to evaporating droplets that contain particles with antibodies for target proteins. The resulting deposition patterns and the voltages required to achieve such patterns will indicate whether or not a protein is present and in what amount. Manufacturing of such a device relies on a firm understanding of colloidal transport in an evaporating droplet and the interplay between the evaporative and electrowetting forces at the contact line, as well as the electrophoretic force on charged colloids. To better analyze the interplay between forces and their effects on colloidal transport, we supplement the experimental work of the DMFL with a mathematical model. The model comprises three coupled pieces: droplet dynamics, particle dynamics, and electrostatics. The first piece of the model will solve for the fluid velocity field in the absence of particles and an electric field. The flow will be solved for both a pinned and moving contact line. The second piece accounts for particle dynamics. The third piece accounts for the application of an electric field. Model predictions will be compared to the experimental data collected by the DMFL [4]. Explanation of experimental procedures and current findings can be found in [5] and [6].

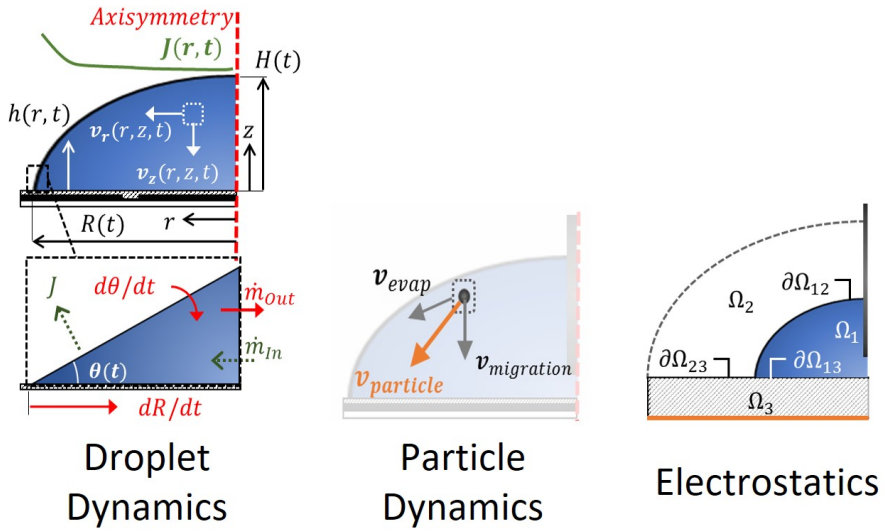

Figure 2: Breakdown of the three-stage coupled model. The first stage captures fluid dynamics. The second stage captures particle dynamics. The third stage captures the effects of an electric field on both fluid flow and particle transport.

In this thesis, we lay the foundation for the three-part coupled model. We present a model for the fluid flow (in the absence of particles and an electric field) inside an axisymmetric droplet of Newtonian fluid with a pinned contact line. We assume the evaporation rate increases as the contact line is approached. At this initial stage in the modeling process, we ignore temperature changes and Marangoni flow, but would like to study Marangoni effects as our research progresses. We further assume the droplet is small enough to neglect gravitational effects.

I.2 Literature Review and Research Goals

Several researchers have previously modeled evaporating droplets. For an extensive review of the contributions to this field, we refer readers to [20] and [26]. In this section, we briefly review a few of these research efforts most relevant to this work before discussing our particular modeling approach.

The theory behind the coffee-ring effect was pioneered by Deegan and coworkers who considered a pinned droplet of solute acting under diffusion-limited evaporation in ambient conditions. They employed several simplifications to characterize the height-averaged velocity, $\bar{v}$, the evaporative flux, $J(r,t)$, and the height of the droplet, $h(r,t)$. They computed approximations for the mass growth of the ring as well as the distribution of the solute. For early times, they predicted the ring grows as a power law in time. The growth at later times is impacted by the assumption of diffusion-limited evaporation. This assumption results in a diverging evaporation rate at the contact line, which leads to both the velocity at the contact line and the growth of the ring diverging. They conclude the divergent behavior at the end of the drying time is responsible for the 100% transfer of solute to the periphery.

Hu and Larson solved for the full field flow inside of a pinned evaporating droplet, first neglecting Marangoni flow [15], which results from surface tension gradients, and then later accounting for it [16]. They developed a semi-analytical lubrication model for which they borrowed the evaporative flux expression presented by Deegan et al. They compared their findings to numerical results of a finite element method developed to solve simultaneously the vapor concentration and the flow field. They concluded that the lubrication model yields a successful approximation of the velocity field for contact angles up to 40°. However, they accounted for the singularity at the contact line by including higher order terms that would be neglected in a standard lubrication approximation.

Masoud and Felske [22] found a full analytical solution for the flow inside a droplet by assuming

Stokes flow in the entire spherical-cap shaped droplet. In order to do so, they modified the evaporative flux expression proposed by Deegan et al. such that the expression is bounded at the contact line.

Maki and Kumar used lubrication theory to model colloidal transport in an evaporating droplet [21]. The research effort focused on identifying the mechanism causing larger-sized particles to migrate to the top of the droplet and form a skin during evaporation. They considered a moving contact line replaced by a thin precursor film, as lubrication theory breaks down in the contact line region when the contact line is pinned and evaporating. In this project, we seek a method of modeling the pinned contact line building off the work of Maki and Kumar.

Other research projects have focused specifically on contact line dynamics, using a wedge to describe the region sufficiently close to the contact line [13, 17, 23]. In [23], Moffatt studied the Stokes flow in a wedge region bounded by two planes, considering both rigid and free surfaces. Their work largely focused on the formation of eddies for small enough contact angles. Gelderblom et al. studied the Stokes flow in a pinned wedge region bounded by a rigid substrate and a free liquid-air interface [13]. They found a full analytical solution for the stream function, assuming evaporative-driven flow. For the evaporative flux, they used the expression given by Deegan et al. Huh and Scriven studied the Stokes flow inside a wedge region with a moving contact line [17].

In this thesis project, we seek to marry the models proposed in [21] and [13]. Maki and Kumar were unable to use full lubrication theory to capture the dynamics of a pinned contact line. We propose amending this issue by linking the analytical wedge model developed by Gelderblom et al. to a modified version of the lubrication model proposed by Maki and Kumar.

We pose two research questions:

(i) Is it possible to describe the fluid dynamics of a pinned evaporating droplet in the lubrication limit using a wedge in the vicinity of the contact line?

(ii) Is it sufficient to link the two models described in [13] and [21] by specifying height and flux conditions at some boundary?

The first question is broad while the second one is the specific strategy we present in this project. We will return to these questions in Section VII.

I.3 Modeling Strategy

We consider an evaporating axisymmetric droplet of Newtonian fluid characterized by cylindrical coordinates (r', z', ω). The droplet rests on a substrate, $z' = 0$, and is centered at the origin, $r' = 0$. The interface, described by $z' = h'(r', t')$, is in contact with ambient air. The contact line is pinned at $r' = R'$, where R' is the radius of the droplet. Note primes denote dimensional values. We split the droplet into two regions by introducing a new boundary at $r' = R' - R'_w$, where R'_w is a small distance from the contact line. The first region, referred to as the droplet region, or full drop region, is characterized by $\Omega'_d(t') = \{(r', z', \omega) : 0 \leq r' \leq R' - R'_w,\ 0 \leq z' \leq h'(r', t'),\ 0 \leq \omega \leq 2\pi\}$. To model this region, we apply lubrication theory to the full Navier-Stokes equations to obtain a simplified interface evolution equation, as done by Maki and Kumar in [21]. The second region, referred to as the contact line region, or wedge region, is characterized by $\Omega'_c(t') = \{(r', z', \omega) : R' - R'_w \leq r' \leq R' \text{ and } 0 \leq z' \leq h'(r', t'),\ 0 \leq \omega \leq 2\pi\}$. Here, we assume Stokes flow, as was done by Gelderblom et al. in [13]. We choose the length R'_w to be small enough that the contact line region looks like a wedge with length R'_w and height $z' = R'_w \tan\theta(t')$ at $r' = R' - R'_w$, where $\theta(t')$ is the contact angle. We introduce a polar coordinate system $(\hat{r}', \phi)$ to describe the location inside of the wedge, which we discuss in Section III. After modeling each region separately, we connect them by assuming both the height and the volumetric flux are continuous at the boundary $r' = R' - R'_w$, where both the height and the volumetric flux are determined by the wedge model.

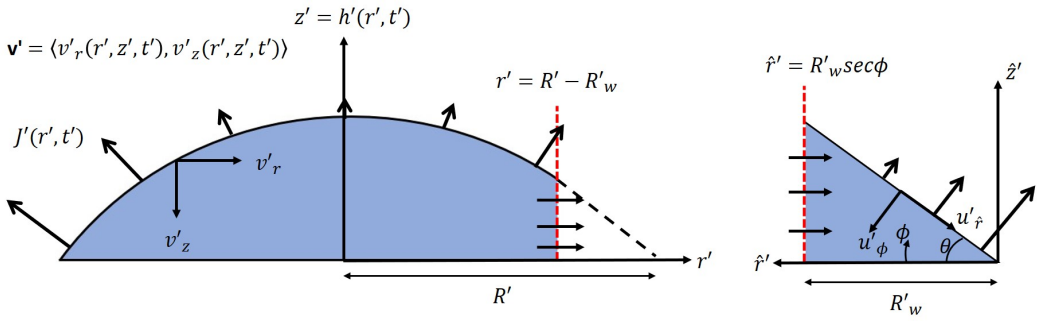

Figure 3: Schematic of the droplet region, $\Omega'_d(t')$, and the contact line region, $\Omega'_c(t')$.

In what follows, we explain how the droplet region is modeled in Section II; we explain how the contact line region is modeled and discuss the wedge flow in Section III; we explain how the two regions are connected in Section IV; and we discuss the results obtained by our numerical simulations in Section VI. Though fluid flow has been modeled in both evaporating droplets and

wedge regions prior to this work, to the best of our knowledge, the two types of models have never been connected.

II. Model Formation: Full Drop Region

To model the full drop region, we apply lubrication theory to the Navier-Stokes equations, as was done by Maki and Kumar in [21]. Lubrication theory is based on the assumption that the contact angle is very small (typically, $\leq 15^\circ$), resulting in a thin, pancake-like droplet in which the height dimension, H', is much smaller than the length dimension, R', as depicted in Figure 4. The disparity in length scales renders the radial derivatives in the Navier-Stokes equations negligible relative to the vertical derivatives, which allows us to neglect them. This will be explained in detail in Section II.2. Though lubrication theory is based on the assumption of a small contact angle, it has been shown to yield a decent approximation to the solution of the Navier-Stokes equations for larger angles. Hu and Larson successfully applied lubrication theory up to a contact angle of $\theta = 40^\circ$ [15]. Thus, we consider $\theta \leq 40^\circ$. Since we are considering an axisymmetric drop, it is enough to model the profile of the droplet. We use cylindrical coordinates, (r', z'), to describe each position in the droplet profile, where $z' = h'(r', t')$ describes the interface with the air and $r' = R' - R'_w$ is the location of the boundary between the full drop and the contact line region. The velocity field is denoted by $\mathbf{v}' = (v'_r, v'_z)$, where v'_r is the radial velocity and v'_z is the vertical velocity. To simulate the droplet evaporating, we need to know the interface evolution equation, $\frac{\partial h'}{\partial t'}$, which describes how the interface changes over time. In this section, we discuss the governing system of equations and scale factors by which we obtain the dimensionless interface evolution equation.

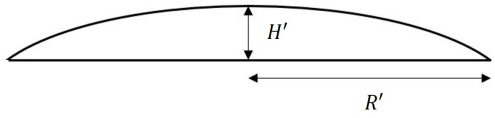

Figure 4: Thin droplet in which there is a disparity between the height scale, H', and the length scale R'.

II.1 Governing Equations and Boundary Conditions

In our system, both mass and momentum must be conserved. Conservation of mass is expressed by the 2-D continuity equation in cylindrical coordinates:

$$\frac{\partial \rho}{\partial t'} + \nabla' \cdot (\rho \mathbf{v}') = 0. \tag{II.1}$$

We assume the droplet fluid is incompressible; thus, the density, ρ, of the liquid is unaffected by pressure and remains constant throughout the drop. The result is the simplified continuity equation:

$$\nabla' \cdot \mathbf{v}' = 0. \tag{II.2}$$

Momentum is conserved when the rate of change of the momentum of the fluid inside the droplet balances the forces acting upon the droplet. In short, it is Newton's second law, $F = ma$. There are two flavors of forces that could act upon the droplet, (i) body forces, which act equally upon the entire body of the droplet (gravity, for example), and (ii) surface forces, which act upon external and internal surfaces and can vary throughtout the droplet (viscosity, for example). Conservation of momementum is expressed by the 2-D Navier-Stokes equations in cylindrical coordinates:

$$\rho \left(\frac{\partial \mathbf{v}'}{\partial t'} + (\mathbf{v}' \cdot \nabla')\mathbf{v}' \right) = -\nabla' p' + \mu \Delta' \mathbf{v}' + f', \tag{II.3}$$

where $\nabla' = \frac{1}{r'} \frac{\partial}{\partial r'}(r') + \frac{\partial}{\partial z'}$ is the gradient, $\Delta' = \nabla'^2 = \frac{1}{r'} \frac{\partial}{\partial r'}(r' \frac{\partial}{\partial r'}) + \frac{\partial^2}{\partial z'^2}$ is the Laplace operator, p' is the pressure, μ is the viscosity of the fluid, and f' represents body forces. The left side of the equation represents the rate of change of the momentum while the right side describes the total surface and body forces, where the terms $-\nabla' p'$ and $\mu \Delta' \mathbf{v}'$ capture the contributions from pressure and viscosity. In our problem, we assume the droplet is thin enough to neglect gravitational forces and we do not account for any other body forces. Thus, on the right-hand side of equation II.3, we retain only the surface forces from pressure and viscosity.

At the substrate, $z' = 0$, we impose no-slip and impermeability conditions. That is, the velocity of the fluid along the substrate must match the velocity of the substrate and cannot pass through it. Hence, our first two boundary conditions are given by

$$v_r'(r', 0, t') = 0, \quad v_z'(r', 0, t') = 0. \tag{II.4}$$

We discussed earlier that surface forces act upon different surfaces throughout the droplet. A surface force can be applied in a direction normal to the surface or in a direction tangent to the surface. At the interface, $z' = h'(r', t')$, we balance the normal and tangential stresses, but, before

doing so, we define the unit vectors in both the normal and tangential directions. To define the unit normal vector, $\mathbf{n}'$, we let $f'(r', z', t') = z' - h'(r', t')$. Thus, the unit normal vector to the interface is

$$\mathbf{n}' = \frac{\nabla' f'}{\|f'\|} = \frac{(-\partial h'/\partial r', 1)}{\sqrt{(\partial h'/\partial r')^2 + 1}}. \tag{II.5}$$

To define the unit tangent vector, $\mathbf{t}'$, we use the knowledge that $\mathbf{t}' \cdot \mathbf{n}' = 0$. Then,

$$\mathbf{t}' = \frac{(1, \partial h'/\partial r')}{\sqrt{(\partial h'/\partial r')^2 + 1}}. \tag{II.6}$$

We also introduce the stress tensor,

$$\mathbf{T}' = -p'\mathbf{I} + \mu(\nabla'\mathbf{v}' + \nabla'\mathbf{v}'^T), \tag{II.7}$$

which contains the stresses from pressure and viscosity, where $\mathbf{I}$ is the 2-D identity tensor and T represents the transpose. The stress at the interface is obtained by performing the dot product of the stress tensor and the unit normal, $\mathbf{T}' \cdot \mathbf{n}'$. The stress occurring in the normal direction is then $\mathbf{n}' \cdot \mathbf{T}' \cdot \mathbf{n}'$. The pressure difference along the droplet interface is related to its shape through surface tension. Thus, the difference in pressure at any point along the interface is given by the term $\kappa\sigma$, where κ is the curvature and σ is the surface tension. Balancing the stress in the normal direction with the pressure from curvature as well as the ambient air pressure, p'_a, we get,

$$-p'_a - \mathbf{n}' \cdot \mathbf{T}' \cdot \mathbf{n}' = -\kappa\sigma, \tag{II.8}$$

where the curvature is expressed as

$$\kappa = \nabla' \cdot [(1 + |\nabla' h'|^2)^{-1/2} \nabla' h']. \tag{II.9}$$

The stress occurring tangent to the interface is obtained by dotting the stress at the interface with the unit tangent vector. We assume the tangential stress, or shear stress, is zero because our experiments are conducted in a lab where there is very little motion of the air surrounding the droplet. Note we are also neglecting Marangoni effects. Thus,

$$\mathbf{t}' \cdot \mathbf{T}' \cdot \mathbf{n}' = 0. \tag{II.10}$$

We also specify a kinematic condition, which states that the vertical velocity at the interface, $v'_z(r', h'(r', t'))$, is determined by the rate at which mass is lost due to evaporation along the surface and also by the rate at which the interface collapses, $\frac{\partial h'}{\partial t'}$. It is given by,

$$J' = \rho(\mathbf{v}' - \mathbf{v}'_\mathbf{I}) \cdot \mathbf{n}', \tag{II.11}$$

where $\mathbf{v}'_\mathbf{I} = (0, \partial h'/\partial t')$ is the velocity of the interface and the evaporative flux (defined as the mass lost due to evaporation per unit area per unit time) is [9, 15, 27]

$$J'(r', t') = \rho J'_0(\theta)(R' - (r')^2)^{\lambda_F(\theta)-1}, \tag{II.12}$$

where [13]

$$\lambda_F(\theta) = \frac{\pi}{2\pi - 2\theta} \tag{II.13}$$

and [14, 15]

$$J_0(\theta) = \frac{Dc_s(1-H)}{R'}(0.27\theta^2 + 1.30)(0.6381 - 0.2239(\theta - \frac{\pi}{4})^2), \tag{II.14}$$

where D is the diffusion constant for water vapor in air, c_s is the saturated vapor concentration at the surface of the droplet, and H is the relative humidity. Values for these parameters can be found in Table 2. Note that $J'(r', t')$ is time dependent because of its dependence on the contact angle, which changes as the drop evaporates over time.

The expression for the evaporative flux is based on the assumption that the vapor concentration, c, in the air surrounding the droplet is diffusion-limited. Generally, an advection-diffusion equation would be used to solve for the vapor concentration. However, we assume the air velocity is negligible and that, far from the droplet interface, the concentration approaches a constant vapor density, c_∞. Along the droplet interface, assumed to be a spherical-cap shape, it is assumed that the vapor concentration is at the saturation concentration, c_s. Thus, the steady-state advection-diffusion equation reduces to Laplace's equation, $\Delta' c = 0$. Knowing the concentration, one can obtain an exact analytical form for the evaporative flux along the entire surface of the droplet using the relation $J'(r', t') = -D(\mathbf{n}' \cdot \nabla' \mathbf{c})$. This calculation has been done in prior work [9, 27]. The exact form for $J'(r', t')$ obtained by solving Laplace's equation contains special functions and

is not user friendly, thus researchers typically use an approximate expression for the evaporative flux. The form we use in equation II.12 is a simplification suggested by Deegan et al. in [8].

Before non-dimensionalizing, we summarize our system of governing equations and boundary conditions:

$$\nabla' \cdot \mathbf{v}' = 0,$$

$$\rho\left(\frac{\partial \mathbf{v}'}{\partial t'} + (\mathbf{v}' \cdot \nabla')\mathbf{v}'\right) = -\nabla' p' + \mu \Delta' \mathbf{v}' + f',$$

$$v_r'(r', 0, t') = 0, \quad v_z'(r', 0, t') = 0,$$

$$-p_a' - \mathbf{n}' \cdot \mathbf{T}' \cdot \mathbf{n}' = -\kappa\sigma,$$

$$\mathbf{t}' \cdot \mathbf{T}' \cdot \mathbf{n}' = 0,$$

and

$$J' = \rho(\mathbf{v}' - \mathbf{v}_\mathbf{I}') \cdot \mathbf{n}'.$$

II.2 Non-dimensionalization

To simplify the governing equations, we assume the droplet is thin such that $\epsilon = \frac{H'}{R'} << 1$, allowing for the application of lubrication theory. Our choice for ϵ is based on the capillary number,

$$Ca = \frac{\mu V'}{\sigma}, \tag{II.15}$$

where $V' = \frac{Dc_s(1-H)}{\rho R'}$ is the characteristic velocity. We base the velocity scale on the rate at which vapor diffuses from the surface of the drop into air. The capillary number is the ratio of viscous effects to surface tension effects. Thus, $Ca << 1$ indicates that surface tension effects dominate and the droplet interface will maintain a spherical cap shape. The capillary number is usually

on the order of 10^{-6} or smaller. Hence, a commonly used simplification of the droplet modeling problem is to derive the interface evolution equation from the equation of a spherical cap, as was done in [8, 9, 14, 15]. In [21], Maki and Kumar were interested in exploring results when surface tension and viscosity effects are equally important, and according to Ajaev [1], this happens when $\epsilon = \frac{H'}{R'} = O(Ca^{1/3})$. Thus, as done by Maki and Kumar, we expand our system of equations in powers of $\epsilon = Ca^{1/3}$.

We non-dimensionalize the governing system of equations with the following scales described in Tables 1 and 2:

$$\begin{aligned} r' = R'r,\ z' = \epsilon R'z,\ h' = \epsilon R'h, \\ v_r' = V'v_r,\ v_z' = \epsilon V'v_z,\ t' = \frac{R'}{V'}t, \\ p' = \frac{\mu V'}{\epsilon^2 R'}p,\ J' = \rho V'\epsilon J. \end{aligned} \tag{II.16}$$

Standard Parameter Values for Water		
Description:	**Value:**	**Related Citation(s):**
Dynamic viscosity	$\mu = 9 \times 10^{-4}$ Pa s	[21]
Density	$\rho = 997$ kg/m^3	[21]
Surface tension	$\sigma = 7.2 \times 10^{-2}$ N/m	[21]
Diffusion coefficient for vapor in air	$D = 3 \times 10^{-5}$ m^2/s	[7]

Table 1: Standard values for water

Characteristic Scales		
Description:	**Value:**	**Related Citation(s):**
Saturated water vapor concentration	$c_s = 0.0232$ kg/m^3	[14]
Relative humidity	$H = 0.4$ kg/m^3	[14]
Length of the droplet radius	$R' = 1 \times 10^{-3}$ m	DMFL, [13]
Characteristic velocity	$V' = \frac{Dc_s(1-H)}{\rho R'} = 4.19 \times 10^{-7}$ m/s	[13, 14, 15]

Table 2: Values associated with characteristic scales

Returning to the conservation of mass equation (II.2), we expand and substitute in the scales to obtain,

$$\frac{V'}{R'}\left[\frac{\partial v_r}{\partial r}+\frac{1}{r}v_r+\frac{\partial v_z}{\partial z}\right]=0. \tag{II.17}$$

Turning our attention to the conservation of momentum equation (II.3), we expand both the radial and vertical components and substitute in the scales to obtain,

$$\frac{\epsilon^2\rho R'V'}{\mu}\left(\frac{\partial v_r}{\partial t}+v_r\frac{\partial v_r}{\partial r}+v_z\frac{\partial v_r}{\partial z}\right)=-\frac{\partial p}{\partial r}+\epsilon^2\left(\frac{1}{r}\frac{\partial}{\partial r}\left(r\frac{\partial v_r}{\partial r}\right)+\frac{1}{\epsilon^2}\frac{\partial^2 v_r}{\partial z^2}-\frac{v_r}{r^2}\right) \tag{II.18}$$

and

$$\frac{\epsilon^4\rho R'V'}{\mu}\left(\frac{\partial v_z}{\partial t}+v_r\frac{\partial v_z}{\partial r}+v_z\frac{\partial v_z}{\partial z}\right)=-\frac{\partial p}{\partial z}+\epsilon^4\frac{1}{r}\frac{\partial}{\partial r}\left(r\frac{\partial v_z}{\partial r}\right)+\epsilon\frac{\partial^2 v_z}{\partial z^2}. \tag{II.19}$$

The left side of the Navier-Stokes equations is multiplied by the Reynolds number, $Re=\frac{\rho R'V'}{\mu}$, which is the ratio of inertial forces to viscous forces. In our problem, $Re\approx 4.6\times 10^{-4}<<1$. Thus, viscosity dominates and the momentum in the drop is close to zero, resulting in a smooth, laminar flow.

Returning to the boundary conditions, we expand the normal and tangential stresses at the interface and the kinematic condition (eqs II.8, II.10, II.11), and substitute in scales to get,

$$-p_a-\frac{1}{\ell_s^2}\left[\left(\epsilon\frac{\partial h}{\partial r}\right)^2\left(-p+2\epsilon^2\frac{\partial v_r}{\partial r}\right)+2\epsilon\frac{\partial h}{\partial r}\left(\epsilon\frac{\partial v_r}{\partial z}+\epsilon^3\frac{\partial v_z}{\partial r}\right)-p-2\epsilon^2\frac{\partial v_z}{\partial z}\right]=-\frac{1}{\ell_s}\left(\frac{\partial^2 h}{\partial r^2}+\frac{1}{r}\frac{\partial h}{\partial r}\right), \tag{II.20}$$

$$-\frac{1}{\ell_s^2}\left[\epsilon\frac{\partial h}{\partial r}\left(-p+2\epsilon^2\frac{\partial v_r}{\partial r}\right)-\left(\frac{\partial v_r}{\partial z}+\epsilon^2\frac{\partial v_z}{\partial r}\right)+\epsilon^2\left(\frac{\partial h}{\partial r}\right)^2\left(\frac{\partial v_r}{\partial z}+\epsilon^2\frac{\partial v_z}{\partial r}\right)-\epsilon\frac{\partial h}{\partial r}\left(-p+2\epsilon^2\frac{\partial v_z}{\partial z}\right)\right]=0, \tag{II.21}$$

and

$$\epsilon V'J=-\epsilon V'\frac{v_r}{\ell_s}\frac{\partial h}{\partial r}+\frac{1}{\ell_s}\left(\epsilon V'v_z-\epsilon V'\frac{\partial h}{\partial t}\right), \tag{II.22}$$

where $\ell_s=\left(\left(\epsilon\frac{\partial h}{\partial r}\right)^2+1\right)^{1/2}$.

We are interested in studying the limit of the scaled system of equations as $\epsilon \to 0$. Taking the limit, we obtain the leading order equations, which lead to our boundary value problem in Section II.3:

$$0 = \frac{1}{r}\frac{\partial}{\partial r}(rv_r) + \frac{\partial v_z}{\partial z} \tag{II.23}$$

$$0 = -\frac{\partial p}{\partial r} + \frac{\partial^2 v_r}{\partial z^2} \tag{II.24}$$

$$0 = -\frac{\partial p}{\partial z} \tag{II.25}$$

with

$$v_r = 0, \quad v_z = 0 \tag{II.26}$$

at $z = 0$, and

$$p = p_a - \frac{1}{r}\frac{\partial}{\partial r}\left(r\frac{\partial h}{\partial r}\right), \tag{II.27}$$

$$\frac{\partial v_r}{\partial z} = 0, \tag{II.28}$$

$$J = -v_r\frac{\partial h}{\partial r} + v_z - \frac{\partial h}{\partial t} \tag{II.29}$$

at $z = h(r,t)$.

II.3 Derivation of Evolution Equation

To obtain the radial velocity, we integrate the radial component of the momentum conservation equation (II.24) twice, using the fact that $\frac{\partial p}{\partial z} = 0$, and apply the tangential stress condition (II.27) at the interface and the no-slip condition (II.26) at the substrate [21]:

$$v_r = \frac{\partial p}{\partial r}\int_0^z (z-h)\,dz = \frac{\partial p}{\partial r}\left(\frac{z^2}{2} - hz\right). \tag{II.30}$$

To get the vertical velocity, we integrate the conservation of mass equation II.23:

$$v_z = -\int_0^z \frac{1}{r}\frac{\partial}{\partial r}(r v_r)\, dz. \tag{II.31}$$

Applying the radial and vertical velocities to the kinematic equation (II.29), we obtain the interface evolution equation:

$$\frac{\partial h}{\partial t} = -\frac{1}{r}\frac{\partial}{\partial r}(rQ) - J \tag{II.32}$$

where

$$Q = \int_0^h v_r dz = \int_0^h \left[\frac{\partial p}{\partial r}\int_0^z (z-h)\right] dz = -\frac{h^3}{3}\frac{\partial p}{\partial r} \tag{II.33}$$

is the volumetric flux and the pressure, p, is given by equation II.27.

It is the evolution equation, derived using the lubrication approximation, we wish to solve using information from the separate model for the contact line region.

III. Model Formation: Contact Line Region

In the model of the contact line region, we consider the base of the wedge to be a small length, R'_w, which is loosely chosen such that the contact line region can be reasonable approximated by a wedge. At this early stage of our research, we are not concerned with the precise location of R'_w, though it would be interesting to vary the length of the wedge and study its impact on our solution. In the wedge coordinate system, the contact line is placed at the origin and each position in the wedge is described by its polar coordinate $(\hat{r}', \phi)$. The contact angle is denoted $\theta(t')$ and decreases due to evaporation at the rate $\frac{d\theta}{dt'}$; therefore, the domain characterizing the wedge is given by $0 \leq \hat{r}' \leq R'_w \sec\phi$ and $0 \leq \phi \leq \theta(t')$, where $\theta(t') \leq \frac{2\pi}{9}$. Note $\frac{2\pi}{9}$ is equivalent to 40°, which is the maximum angle we consider based on accuracy deduced from prior literature [15]. The velocity field consists of a radial component and an angular component and is denoted $\mathbf{u'} = (u'_{\hat{r}}, u'_\phi)$.

III.1 Governing Equations

As in the full drop region, both mass and momentum must be conserved. Conservation of mass in the contact line region is expressed as the 2-D continuity equation in polar coordinates:

$$\frac{1}{\hat{r}'}\frac{\partial}{\partial \hat{r}'}(\hat{r}' u'_{\hat{r}}) + \frac{1}{\hat{r}'}\frac{\partial}{\partial \phi}(u'_{\phi}) = 0. \tag{III.1}$$

Since we assume laminar flow based on the Reynolds number, we can simplify the dimensional Navier-Stokes to the Stokes equations:

$$0 = -\frac{\partial \hat{p}'}{\partial \hat{r}'} + \mu\left(\Delta' u'_{\hat{r}} - \frac{u'_{\hat{r}}}{\hat{r}'^2} - \frac{2}{\hat{r}'^2}\frac{\partial u'_{\phi}}{\partial \phi}\right) \tag{III.2}$$

$$0 = -\frac{1}{\hat{r}'}\frac{\partial \hat{p}'}{\partial \phi} + \mu\left(\Delta' u'_{\phi} - \frac{u'_{\phi}}{\hat{r}'^2} + \frac{2}{\hat{r}'^2}\frac{\partial u'_{\hat{r}}}{\partial \phi}\right) \tag{III.3}$$

Here we note some comparisons between the simplified Navier-Stokes equations used to model the full drop region and the Stokes equations. The flow in the full drop is also laminar, which was captured by the application of lubrication theory. Recall that the changes in momentum were neglected (equations II.24, II.25). When we applied lubrication theory to the Navier-Stokes equations, we lost the r derivatives in the viscosity term. In the assumption of a thin droplet, the disparity between the height and length scales renders the r derivatives insignificant relative to the z derivatives. However, close to the contact line, the disparity in scales is lost and all terms become equally important. This is captured by equations III.2 and III.3.

To solve the Navier-Stokes equations, we introduce the stream function, $\psi'(\hat{r}', \phi, t')$, which provides the flow trajectories. The radial and angular velocities are defined in terms of the stream function as

$$u'_{\hat{r}} = -\frac{1}{\hat{r}'}\frac{\partial \psi'}{\partial \phi}, \quad u'_{\phi} = \frac{\partial \psi'}{\partial \hat{r}'}, \tag{III.4}$$

which are chosen to satisfy the continuity equation. Thus, once the stream function is known, the velocity field can be obtained.

Substituting in equation III.4 into equations III.2 and III.3 and combining equations III.2 and III.3 such that the pressure terms are eliminated, the Stokes equations can be expressed in terms of the stream function by the biharmonic equation,

$$\nabla'^4 \psi' = 0, \tag{III.5}$$

which, when solved using separation of variables, yields the general form of the stream function:

$$\psi'(\hat{r}', \phi, t') = \hat{r}'^{\lambda}\{A\cos(\lambda\phi) + B\sin(\lambda\phi) + C\cos[(\lambda-2)\phi] + D\sin[(\lambda-2)\phi]\}, \tag{III.6}$$

where A, B, C, and D are time-dependent constants found by applying the boundary conditions discussed in Section III.2, and $\lambda \neq 0, 1, 2$ is a constant.

Values of $\lambda = 0, 1, 2$ give rise to the following degenerate solutions of the stream function [23]:

$$\psi'(\hat{r}', \phi, t') = [A + B\phi + C\phi^2 + D\phi^3], \text{ if } \lambda = 0, \tag{III.7}$$

$$\psi'(\hat{r}', \phi, t') = \hat{r}'[A\cos\phi + B\sin\phi + C\phi\cos\phi + D\phi\sin\phi], \text{ if } \lambda = 1, \tag{III.8}$$

$$\psi'(\hat{r}', \phi, t') = \hat{r}'^2[A\cos(2\phi) + B\sin(2\phi) + C\phi + D], \text{ if } \lambda = 2. \tag{III.9}$$

III.2 Boundary Conditions

At the substrate, we impose no-slip and impermeability conditions:

$$u'_{\hat{r}}(\hat{r}', 0, t') = -\frac{1}{\hat{r}'}\frac{\partial\psi'}{\partial\phi}\bigg|_{\phi=0} = 0, \quad u'_{\phi}(\hat{r}', 0, t') = \frac{\partial\psi'}{\partial\hat{r}'}\bigg|_{\phi=0} = 0. \tag{III.10}$$

At the liquid-air interface, we assume the shear stress is zero, as was done in the full drop. This yields,

$$\tau'_{\hat{r}\phi}\bigg|_{\phi=\theta} = \mu\left[\hat{r}'\frac{\partial}{\partial\hat{r}'}\left(\frac{1}{\hat{r}'}\frac{\partial\psi'}{\partial\hat{r}'}\right) - \frac{1}{\hat{r}'^2}\frac{\partial^2\psi'}{\partial\phi^2}\right] = 0. \tag{III.11}$$

Lastly, we specify the kinematic condition:

$$u'_{\phi}(\hat{r}', \theta, t') = \frac{\hat{J}'(\hat{r}', t')}{\rho} + \frac{d\theta}{dt'}\hat{r}', \tag{III.12}$$

where the evaporative flux in the vicinity of the contact line is defined by

$$\hat{J}'(\hat{r}', t') = \rho V' J_0(\theta) \left(\frac{\hat{r}'}{R'}\right)^{\lambda_F(\theta)-1}, \tag{III.13}$$

with dimensionless $J_0(\theta) = (0.27\theta^2 + 1.30)(0.6381 - 0.2239(\theta - \frac{\pi}{4})^2)$ and λ_F defined in equation II.13.

The kinematic condition states that the angular velocity at the interface is determined both by the rate at which mass is lost due to evaporation at the surface and also by the rate, $\frac{d\theta}{dt'}$, at which the interface collapses. In order to determine an analytical expression for this rate, the volume of the droplet must be known. In prior research efforts, the droplet interface was assumed to maintain a spherical cap shape over the entire evaporation period and $\frac{d\theta}{dt'}$ was determined by performing a mass balance ([9, 13, 27]). Without making such an assumption, the interface position and the angle would have to be solved for simultaneously. In this thesis project, we do not wish to assume the interface maintains the shape of a spherical cap. However, at this early stage in our research, we also do not wish to fully couple our models for the full drop and contact line regions. Instead, we use an observational rate of change. In dimensional form,

$$\frac{d\theta}{dt'} = -\beta(\theta)\frac{V'}{R'} \tag{III.14}$$

where β is a constant determined by fitting a linear curve to data provided by the DMFL at RIT. Note the rate at which the interface collapses sets the time scale for the entire droplet.

In the full drop region, we defined the evaporative flux by equation II.12, which is an approximation of the full analytical expression found by solving the vapor density problem. Deegan and coworkers claim that in the vicinity of the contact line, the evaporative flux becomes

$$J' = \rho V' J_0 \left(1 - \frac{r'}{R'}\right)^{\lambda_F(\theta)-1}. \tag{III.15}$$

Notice equation III.13 is equivalent to expression III.15, but defined using our contact line region coordinate system. In equation III.13, if the contact angle $\theta < \frac{\pi}{2}$ radians, then $\lambda_F(\theta) < 1$. This means the exponent in equation III.13 will be negative, placing $\hat{r}'$ in the denominator of the expression. Because we placed the contact line of the wedge at the origin in our coordinate system,

as the contact line is approached, $\hat{r}' \to 0$. So, for $\theta < \frac{\pi}{2}$, as $\hat{r}' \to 0$, the expression $\hat{J}'(\hat{r}', t')$ blows up. This captures the idea that as the contact line is approached, the evaporation rate increases, though this is only true when the contact angle is less than $\frac{\pi}{2}$ radians. In order for $\hat{J}'(\hat{r}', t')$ to be functional, it must blow up slowly enough that we can still integrate the expression. We briefly show this is the case by integrating $\hat{J}'(\hat{r}', t')$ from a to $R'_w \sec\theta$ and taking the limit of the integral as a approaches zero:

$$\begin{aligned}\lim_{a\to 0}\int_a^{R'_w\sec\theta}\frac{\hat{J}'(\hat{r}',t')}{\rho}\,d\hat{r}' &= \lim_{a\to 0}\int_a^{R'_w\sec\theta} V'J_0(\theta)\left(\frac{\hat{r}'}{R'}\right)^{\lambda_F(\theta)-1} d\hat{r}' \\ &= \lim_{a\to 0}\left[\frac{V'J_0(\theta)}{R'^{\lambda_F(\theta)-1}}\frac{(R'_w\sec\theta)^{\lambda_F(\theta)}}{\lambda_F(\theta)} - \frac{V'J_0(\theta)}{R'^{\lambda_F(\theta)-1}}\frac{a^{\lambda_F(\theta)}}{\lambda_F(\theta)}\right] \\ &= \frac{V'J_0(\theta)}{R'^{\lambda_F(\theta)-1}}\frac{(R'_w\sec\theta)^{\lambda_F(\theta)}}{\lambda_F(\theta)}.\end{aligned} \tag{III.16}$$

For $\theta > \frac{\pi}{2}$ radians, $\lambda_F(\theta) > 1$ meaning $\hat{r}'$ remains in the numerator of equation III.13. This indicates that when the contact angle of the droplet is above 90°, the evaporation rate actually decreases. This captures the idea that, for large contact angles, as the contact line is approached, there is less ambient air between the droplet interface and the substrate for vapor molecules at the surface of the drop to diffuse into. Recall we only consider contact angles at or below 40°, or $\frac{2\pi}{9}$ radians, since Hu and Larson showed in [15] that the lubrication approximation handles well within this range of contact angles.

In [13], Gelderblom et al. solve for the flow inside of the wedge by considering separately the evaporative contribution, the collapsing interface contribution, and the homogeneous contribution. This can be done because the PDE given in equation III.5 is linear. Splitting up the kinematic condition into these three "sub" boundary conditions and applying each of them to the stream function leads to three different types of solutions: (i) the velocity field due to the evaporative flux, found by applying the condition,

$$u'_\phi(\hat{r}', \theta, t') = \frac{\hat{J}'(\hat{r}', t')}{\rho}; \tag{III.17}$$

(ii) the velocity field due the collapsing interface, found by applying the condition,

$$u'_\phi(\hat{r}', \theta, t') = \frac{d\theta}{dt'}\hat{r}'; \tag{III.18}$$

and (iii) the velocity field that results when there is no evaporation at all, found by applying the homogeneous condition,

$$u'_\phi(\hat{r}', \theta, t') = 0. \tag{III.19}$$

As was done in [13], we henceforth refer to equations III.17, III.18, and III.19 as the flux condition, the hinge condition, and the eigenmode, respectively. Splitting the kinematic condition in this way simplifies analytical calculations while also allowing us to see the effects of the different contributions. The full solution is simply obtained by superposition of the flux, hinge, and eigenmode solutions.

Note that each of these "sub" boundary conditions scale with a different power of $\hat{r}'$. Therefore, each one will give rise to a different power of $\hat{r}'$ in the final solution. Recall the expression for the evaporative flux given in equation III.15 scales as $\hat{r}'^{\lambda_F(\theta)-1}$. Thus, the flux condition scales as $\hat{r}'^{\lambda_F(\theta)-1}$. The hinge condition clearly scales as $\hat{r}'$. The eigenmode solution scales with an exponent denoted λ_E. This exponent depends on the contact angle θ, and is a root of the eigenvalue equation

$$M(\lambda, \theta) = \sin[2(\lambda - 1)\theta] - (\lambda - 1)\sin(2\theta). \tag{III.20}$$

It is not clear why the eigenmode scales the way it does simply by looking at the condition stated in equation III.19. We justify this later in the document when showing how to obtain the eigenmode solution.

III.3 Non-dimensionalization

We non-dimensionalize the governing system of equations and boundary conditions using the following scales:

$$\begin{gathered}\hat{r}' = R'\hat{r},\ u'_{\hat{r}} = V'u_{\hat{r}},\ u'_\phi = V'u_\phi,\ \psi' = R'V'\psi \\ \hat{p}' = \frac{\mu V'}{R'}\hat{p},\ t' = \frac{R'}{V'}t,\ \hat{J}' = \rho V'\hat{J}.\end{gathered} \tag{III.21}$$

Substituting the appropriate scales into the velocity, continuity, and Stokes equations (equations III.1, III.2, III.3, III.4), we find their dimensionless forms:

$$u_{\hat{r}} = -\frac{1}{\hat{r}}\frac{\partial \psi}{\partial \phi}, \quad u_{\phi} = \frac{\partial \psi}{\partial \hat{r}}, \tag{III.22}$$

$$\frac{1}{\hat{r}}\frac{\partial}{\partial \hat{r}}(\hat{r}u_{\hat{r}}) + \frac{1}{\hat{r}}\frac{\partial}{\partial \phi}(u_{\phi}) = 0, \tag{III.23}$$

and

$$0 = -\frac{\partial \hat{p}}{\partial \hat{r}} + \Delta \hat{u}_{\hat{r}} \tag{III.24}$$

$$0 = -\frac{1}{\hat{r}}\frac{\partial \hat{p}}{\partial \phi} + \Delta \hat{u}_{\hat{\phi}}. \tag{III.25}$$

Substituting the appropriate scales into the boundary conditions (equations III.10, III.11, and III.12), we find their dimensionless forms:

$$u_{\hat{r}}(\hat{r}, 0, t) = -\frac{1}{\hat{r}}\frac{\partial \psi}{\partial \phi}\bigg|_{\phi=0} = 0, \quad u_{\phi}(\hat{r}', 0, t) = \frac{\partial \psi}{\partial \hat{r}}\bigg|_{\phi=0} = 0, \tag{III.26}$$

$$\left[\hat{r}\frac{\partial}{\partial \hat{r}}\left(\frac{1}{\hat{r}}\frac{\partial \psi}{\partial \hat{r}}\right) - \frac{1}{\hat{r}^2}\frac{\partial^2 \psi}{\partial \phi^2}\right]\bigg|_{\phi=\theta} = 0, \tag{III.27}$$

and

$$u_{\phi}(\hat{r}, \theta, t) = \hat{f}(\hat{r}, t) + \frac{d\theta}{dt}\hat{r}. \tag{III.28}$$

III.4 Solutions

In [13], Gelderblom and collaborators simply state the solutions they obtained from the flux condition, hinge condition, and the eigenmode. Since we utilize their wedge model, we explain in this section the steps to reproduce their solutions. Recall each condition scales as a different power of $\hat{r}$. Thus, in equation III.6, $\lambda(\theta)$ has a different value when each condition is applied. Each condition is a stipulation on $u_{\phi}(\hat{r}, \theta, t) = \frac{\partial \psi}{\partial r}$. Therefore, for the flux and hinge boundary conditions to hold for all values of $\hat{r}$, $\psi(\hat{r}, t)$ must be the same power function. With this information, we can

determine the value of $\lambda(\theta)$ for the flux and hinge. For the flux, $\lambda(\theta) = \lambda_F(\theta)$, given by equation II.13, and for the hinge, $\lambda(\theta) = 2$. For the eigenmode, the value of $\lambda(\theta) = \lambda_E(\theta)$, which, as stated earlier, is a value that satisfies $M(\lambda, \theta) = 0$. For the flux and eigenmode, we use the general form of the stream function (equation III.6), but for the hinge, we must use the degenerate form given in equation III.9.

III.4.1 Flux solution

To obtain the flux solution, we apply the three boundary conditions stated in equations III.10 and III.11 as well as the flux condition given in equation III.17. Applying the first boundary condition yields,

$$u_{\hat{r}}(\hat{r}, 0, t) = -\frac{1}{\hat{r}} \frac{\partial \psi}{\partial \phi}\bigg|_{\phi=0} = -\hat{r}^{\lambda_F - 1}\{B_F \lambda_F + D_F(\lambda_F - 2)\} = 0, \tag{III.29}$$

where A_F, B_F, C_F, and D_F are the coefficients of the flux stream function.

For $\hat{r} = 0$, equation III.29 is true for all values of the coefficients. For $\hat{r} > 0$, the expression inside of the curly braces must be zero. Then we find B_F in terms of D_F must be

$$B_F = -\frac{D_F(\lambda_F - 2)}{\lambda_F}. \tag{III.30}$$

Applying the second boundary condition, we get

$$u_\phi(\hat{r}, 0, t) = \frac{\partial \psi}{\partial \hat{r}}\bigg|_{\phi=0} = \lambda_F \hat{r}^{\lambda_F - 1}\{A_F + C_F\} = 0. \tag{III.31}$$

Then A_F in terms of C_F is given by

$$A_F = -C_F. \tag{III.32}$$

Applying the third boundary condition, we get

$$\begin{aligned}\tau_{\hat{r}\phi} &= \left[\hat{r}\frac{\partial}{\partial \hat{r}}\left(\frac{1}{\hat{r}}\frac{\partial \psi}{\partial \hat{r}}\right) - \frac{1}{\hat{r}^2}\frac{\partial^2 \psi}{\partial \phi^2}\right]\Bigg|_{\phi=\theta} \\ &= 2(\lambda_F - 1)\hat{r}^{\lambda_F - 2}\{A_F\lambda_F \cos(\lambda_F\theta) + B_F\lambda_F \sin(\lambda_F\theta) + C_F(\lambda_F - 2)\cos[(\lambda_F - 2)\theta] + D_F(\lambda_F - 2)\sin[(\lambda_F - 2)\theta]\} \\ &= 0.\end{aligned} \tag{III.33}$$

For $\hat{r} = 0$, equation III.33 is true for all values of the coefficients. For $\hat{r} > 0$, the expression inside the curly braces must be zero because we know $\lambda_F \neq 1$. Setting the expression equal to zero, we get

$$A_F\lambda_F \cos(\lambda_F\theta) + B_F\lambda_F \sin(\lambda_F\theta) + C_F(\lambda_F - 2)\cos[(\lambda_F - 2)\theta] + D_F(\lambda_F - 2)\sin[(\lambda_F - 2)\theta] = 0. \tag{III.34}$$

Applying the flux condition (III.17),

$$\begin{aligned}u_\phi(\hat{r}, \theta, t) &= \frac{\partial \psi}{\partial \hat{r}}\Bigg|_{\phi=\theta} \\ &= \lambda_F \hat{r}^{\lambda_F - 1}\{A_F \cos(\lambda_F\theta) + B_F \sin(\lambda_F\theta) + C_F \cos[(\lambda_F - 2)\theta] + D_F \sin[(\lambda_F - 2)\theta]\} \\ &= \frac{\hat{J}(\hat{r}, t)}{\rho},\end{aligned} \tag{III.35}$$

which we write as

$$A_F\lambda_F \cos(\lambda_F\theta) + B_F\lambda_F \sin(\lambda_F\theta) + C_F\lambda_F \cos[(\lambda_F - 2)\theta] + D_F\lambda_F \sin[(\lambda_F - 2)\theta] = \frac{\hat{J}(\hat{r}, t)}{\rho\hat{r}^{\lambda_F - 1}}. \tag{III.36}$$

Notice the first two terms of equations III.34 and III.36 are the same. We can eliminate coefficients A_F and B_F by subtracting equation III.34 from III.36. Doing so yields,

$$C_F \cos[(\lambda_F - 2)\theta] + D_F \sin[(\lambda_F - 2)\theta] = \frac{\hat{J}(\hat{r}, t)}{2\rho\hat{r}^{\lambda_F - 1}}, \tag{III.37}$$

which we rewrite as C_F in terms of D_F:

$$C_F = \frac{\hat{J}(\hat{r},t)}{2\rho\hat{r}^{\lambda_F-1}\cos[(\lambda_F-2)\theta]} - D_F\tan[(\lambda_F-2)\theta]. \tag{III.38}$$

Recall from equation III.32 that A_F is related to C_F. If we replace C_F using equation III.38, the result is

$$A_F = D_F\tan[(\lambda_F-2)\theta] - \frac{\hat{J}(\hat{r},t)}{2\rho\hat{r}^{\lambda_F-1}\cos[(\lambda_F-2)\theta]}, \tag{III.39}$$

and now all coefficients are in terms of D_F. To find an expression for D_F, we substitute equations III.30, III.38, and III.39 into equation III.34:

$$\begin{aligned}
&\left\{D_F\tan[(\lambda_F-2)\theta] - \frac{\hat{J}(\hat{r},t)}{2\rho\hat{r}^{\lambda_F-1}\cos[(\lambda_F-2)\theta]}\right\}\lambda_F\cos(\lambda_F\theta) - D_F(\lambda_F-2)\sin(\lambda_F\theta)\\
&+\left\{\frac{\hat{J}(\hat{r},t)}{2\rho\hat{r}^{\lambda_F-1}\cos[(\lambda_F-2)\theta]} - D_F\tan[(\lambda_F-2)\theta]\right\}(\lambda_F-2)\cos[(\lambda_F-2)\theta]\\
&+D_F(\lambda_F-2)\sin[(\lambda_F-2)\theta] = 0,
\end{aligned} \tag{III.40}$$

and solve for D_F to obtain,

$$D_F = \frac{\hat{J}(\hat{r},t)P(\theta)}{2\rho\hat{r}^{\lambda_F-1}}, \tag{III.41}$$

where

$$P(\theta) = \frac{2-\lambda_F+\lambda_F\cos(\lambda_F\theta)\sec[(\lambda_F-2)\theta]}{-(\lambda_F-2)\sin(\lambda_F\theta)+\lambda_F\cos(\lambda_F\theta)\tan[(\lambda_F-2)\theta]}. \tag{III.42}$$

Now that we've obtained an explicit expression for D_F, we can do the same for A_F, B_F, and C_F. Back-substituting equation III.41 into equations III.30, III.38, and III.39, we find,

$$A_F = \frac{\hat{J}(\hat{r},t)P(\theta)}{2\rho\hat{r}^{\lambda_F-1}}\tan[(\lambda_F-2)\theta] - \frac{\hat{J}(\hat{r},t)}{2\rho\hat{r}^{\lambda_F-1}\cos[(\lambda_F-2)\theta]}, \tag{III.43}$$

$$B_F = -\frac{\hat{J}(\hat{r},t)P(\theta)}{2\rho\hat{r}^{\lambda_F-1}}\frac{(\lambda_F-2)}{\lambda_F}, \tag{III.44}$$

and

$$C_F = -\frac{\hat{J}(\hat{r},t)P(\theta)}{2\rho\hat{r}^{\lambda_F-1}}\tan[(\lambda_F-2)\theta] + \frac{\hat{J}(\hat{r},t)}{2\rho\hat{r}^{\lambda_F-1}\cos[(\lambda_F-2)\theta]}. \tag{III.45}$$

To obtain the flux solution, we substitute the coefficients into the general stream function (equation III.6):

$$\begin{aligned}\psi_F(\hat{r},\phi,t) = \frac{\hat{J}(\hat{r},t)}{2\rho\hat{r}^{\lambda_F-1}}\hat{r}_F^{\lambda}\{(P(\theta)\tan[(\lambda_F-2)\theta] - \sec[(\lambda_F-2)\theta])\cos(\lambda_F\phi) - \frac{P(\theta)(\lambda_F-2)}{\lambda_F}\sin[(\lambda_F-2)\phi] \\ + (-P(\theta)\tan[(\lambda_F-2)\theta] + \sec[(\lambda_F-2)\theta])\cos[(\lambda_F-2)\phi] + P(\theta)\sin[(\lambda_F-2)\phi]\}.\end{aligned} \tag{III.46}$$

To write equation III.46 in the form given in [13] requires strategic simplification of the expression inside the curly braces. Showing this rather laborious process is not essential to understanding the flux solution, so we do not show it. We do note that the common denominator of equation III.46 is the eigenmode equation stated in equation III.20.

In simplified form, the flux stream function is

$$\psi_F(\hat{r},\phi,t) = \frac{J_0(\theta)}{M(\lambda_F,\theta)}\hat{r}^{\lambda_F(\theta)}f(\phi,\theta), \tag{III.47}$$

where

$$\begin{aligned}f(\phi,\theta) = \frac{1}{2}[(\lambda_F-2)\{\sin(\lambda_F\theta) - \sin[(\lambda_F-2)\theta]\}\{\cos(\lambda_F\phi) - \cos[(\lambda_F-2)\phi]\} \\ + \{\lambda_F\cos(\lambda_F\theta) - (\lambda_F-2)\cos[(\lambda_F-2)\theta]\}\left\{\sin[(\lambda_F-2)\phi] - \frac{\lambda_F-2}{\lambda_F}\sin\lambda_F\phi\right\}].\end{aligned} \tag{III.48}$$

III.4.2 Hinge solution

To obtain the hinge solution, we apply the three boundary conditions stated in equations III.10 and III.11 as well as the hinge condition given in equation III.18. Applying the first boundary condition to equation III.9, we get,

$$u_{\hat{r}}(\hat{r},0,t) = -\hat{r}(-2A_H\sin 0 + 2B_H\cos 0 + C_H) = 0. \tag{III.49}$$

Then,

$$B_H = -\frac{C_H}{2}. \tag{III.50}$$

Applying the second boundary condition, we get

$$u_\phi(\hat{r}, 0, t) = 2\hat{r}(A_H \cos 0 + B_H \sin 0 + C_H(0) + D_H) = 0. \tag{III.51}$$

Then,

$$A_H = -D_H. \tag{III.52}$$

Applying the third boundary condition, we get

$$\tau_{r\phi}\Big|_{\phi=\theta} = [4(A_H \cos(2\theta) + B_H \sin(2\theta))] = 0, \tag{III.53}$$

hence,

$$A_H \cos(2\theta) + B_H \sin(2\theta) = 0. \tag{III.54}$$

Applying the hinge condition stated in equation III.18, we get

$$A_H \cos(2\theta) + B_H \sin(2\theta) + C_H\theta + D_H = \frac{1}{2}\frac{d\theta}{dt}. \tag{III.55}$$

Note the first two terms of equations III.54 and III.55 are the same. Subtracting equation III.54 from equation III.55, we obtain an expression for D_H in terms of C_H:

$$D_H = \frac{1}{2}\frac{d\theta}{dt} - C_H\theta. \tag{III.56}$$

From equation III.52, we know A_H in terms of D_H. Using equation III.56, we obtain A_H in terms of C_H:

$$A_H = C_H\theta - \frac{1}{2}\frac{d\theta}{dt}. \tag{III.57}$$

Now that we have all coefficients in terms of C_H, we apply the expressions for A_H and B_H to equation III.54, which yields

$$\left(C_H\theta - \frac{1}{2}\frac{d\theta}{dt}\right)\cos(2\theta) - \frac{C_H}{2}\sin(2\theta) = 0. \tag{III.58}$$

Solving for C_H, we obtain the expression

$$C_H = \frac{1}{2\theta - \tan(2\theta)}\frac{d\theta}{dt}. \tag{III.59}$$

Now that we know C_H, we back-substitute to determine A_H, B_H, and D_H:

$$A_H = \left(\frac{\theta}{2\theta - \tan(2\theta)} - \frac{1}{2}\right)\frac{d\theta}{dt}, \tag{III.60}$$

$$B_H = -\frac{1}{2(2\theta - \tan(2\theta))}\frac{d\theta}{dt}, \tag{III.61}$$

and

$$D_H = \left(\frac{1}{2} - \frac{\theta}{2\theta - \tan(2\theta)}\right)\frac{d\theta}{dt}. \tag{III.62}$$

To obtain the hinge solution, we substitute equations III.59, III.60, III.61, and III.62 into equation III.9. Then,

$$\begin{aligned}\psi_H(\hat{r},\phi,t) &= \hat{r}^2\frac{d\theta}{dt}\left[\frac{\tan(2\theta)\cos(2\phi)}{2(2\theta - \tan(2\theta))} - \frac{\sin(2\phi)}{2(2\theta - \tan(2\theta))} + \frac{2\phi - \tan(2\theta)}{2(2\theta - \tan(2\theta))}\right] \\ &= -\hat{r}^2\frac{d\theta}{dt}\frac{1}{2(2\theta - \tan(2\theta))}\left[\sin(2\phi) - \tan(2\theta)\cos(2\phi) - 2\phi + \tan(2\theta)\right].\end{aligned} \tag{III.63}$$

We can write this in condensed form as

$$\psi_H(\hat{r},\phi,t) = \frac{\beta(\theta)}{N(\theta)}\hat{r}^2 g(\phi,\theta), \tag{III.64}$$

where

$$N(\theta) = 2(2\theta - \tan(2\theta)), \tag{III.65}$$

$$g(\phi,\theta) = \sin(2\phi) - \tan(2\theta)\cos(2\phi) - 2\phi + \tan(2\theta), \tag{III.66}$$

and $\beta(\theta) = -\frac{d\theta}{dt}$.

III.4.3 Eigenmode solution

To determine the eigenmode solution, we apply the three boundary conditions given in equations III.10, III.11, and the eigenmode condition (III.19) to the general form of the stream function. We do not show the application of the first three boundary conditions since this was done for the flux. We will obtain the same expressions stated in equations III.30, III.32, and III.34, but we change the notation to indicate we are referring to values associated with the eigenmode solution. Thus,

$$B_E = -\frac{D_E(\lambda_E - 2)}{\lambda_E}, \tag{III.67}$$

$$A_E = -C_E, \tag{III.68}$$

and

$$A_E\lambda_E\cos(\lambda_E\theta) + B_E\lambda_E\sin(\lambda_E\theta) + C_E(\lambda_E - 2)\cos[(\lambda_E - 2)\theta] + D_E(\lambda_E - 2)\sin[(\lambda_E - 2)\theta] = 0. \tag{III.69}$$

Applying the eigenmode condition, we get

$$u_\phi(\hat{r}, \theta, t) = \lambda_E\hat{r}^{\lambda_E - 1}\{A_E\cos(\lambda_E\theta) + B_E\sin(\lambda_E\theta) + C_E\cos[(\lambda_E - 2)\theta] + D_E\sin[(\lambda_E - 2)\theta]\} = 0. \tag{III.70}$$

When $\hat{r} = 0$, the condition is satisfied for all values of the coefficients, so we equate the expression inside the curly braces with zero and obtain

$$A_E\cos(\lambda_E\theta) + B_E\sin(\lambda_E\theta) + C_E\cos[(\lambda_E - 2)\theta] + D_E\sin[(\lambda_E - 2)\theta] = 0. \tag{III.71}$$

Note that the first two terms of equation III.69 and the first two terms of equation III.71 differ by a factor of λ_E. If we multiply both sides of equation III.71 by λ_E and subtract the result from

equation III.69, we can eliminate two of the unknown coefficients. Doing so allows us to obtain an expression for C_E in terms of D_E:

$$C_E = -\frac{D_E \sin[(\lambda_E - 2)\theta]}{\cos[(\lambda_E - 2)\theta]}. \tag{III.72}$$

We now can write all coefficients in terms of D_E by applying equation III.72 to III.68, which yields

$$A_E = \frac{D_E \sin[(\lambda_E - 2)\theta]}{\cos[(\lambda_E - 2)\theta]}. \tag{III.73}$$

Now that we have all coefficients written in terms of D_E, we substitute equations III.67, III.72, and III.73 into equation III.71 to solve for D_E:

$$D_E \left[\frac{\sin[(\lambda_E - 2)\theta]\cos(\lambda_E\theta)}{\cos[(\lambda_E - 2)\theta]} - \frac{(\lambda_E - 2)}{\lambda_E}\sin(\lambda_E\theta)\right] = 0. \tag{III.74}$$

From equation III.74, we see it is impossible to determine a non-trivial value for D_E. However, if we assume $D_E \neq 0$, then the expression inside the bracket of equation III.74 must be zero. Setting this expression to zero and using trig identities to simplify, we obtain

$$\sin[2(\lambda_E - 1)\theta] - (\lambda_E - 1)\sin(2\theta) = 0. \tag{III.75}$$

Note this is the eigenvalue equation stated in equation III.20. From this calculation, we can see why, for the eigenmode, we must choose λ in the stream function to be a value that satisfies $M(\lambda, \theta) = 0$. Otherwise, the eigenmode condition could not be satisfied with a non-zero coefficient, D_E.

Since we have not yet obtained a value for D_E, we write the eigenmode solution in terms of the unknown coefficient by plugging equations III.67, III.72, and III.73 into the stream function. We obtain

$$\begin{aligned}\psi_E(\hat{r}, \phi, t) = D_E(\theta)\hat{r}^{\lambda_E}[&\frac{\sin[(\lambda_E - 2)\theta]}{\cos[(\lambda_E - 2)\theta]}\cos(\lambda_E\phi) - \frac{(\lambda_E - 2)}{\lambda_E}\sin(\lambda_E\phi) - \frac{\sin[(\lambda_E - 2)\theta]}{\cos[(\lambda_E - 2)\theta]}\cos[(\lambda_E - 2)\phi] \\ &+ \sin[(\lambda_E - 2)\phi]],\end{aligned} \tag{III.76}$$

which simplifies to the equation,

$$\psi_E(\hat{r}, \phi, t) = D_E(\theta)\hat{r}^{\lambda_E} h(\phi, \theta) \tag{III.77}$$

where

$$h(\phi, \theta) = \sin[(\lambda_E - 2)(\theta - \phi)] - \frac{\sin[(\lambda_E - 2)\theta]}{\sin(\lambda_E \theta)} \sin[\lambda_E(\theta - \phi)]. \tag{III.78}$$

III.5 Results

III.5.1 Dominant Contribution

As stated earlier, due to the linearity of the partial differential equation, the full solution to the flow in the wedge is obtained by superposition of the flux, hinge, and eigenmode solutions. Which of these pieces dominates near the contact line depends on the scaling with $\hat{r}$. Recall the flux, hinge, and eigenmode scale with $\hat{r}^{\lambda_F}$, $\hat{r}^2$, and $\hat{r}^{\lambda_E}$, respectively. Figure 5 shows the powers of $\hat{r}$ plotted as a function of the contact angle, θ for $0^\circ \leq \theta \leq 180^\circ$. The smallest exponent determines which of the flux, hinge, or eigenmode provides the leading order term. Figure 5 shows the flux dominating for $\theta < 133.4^\circ$, which is well above the maximum contact angle we consider in this project. For $\theta < 79.6^\circ$, the only solutions to equation $M(\lambda, \theta)$ are $\lambda_E = 0, 1, 2$, which all lead to degenerate forms of the stream function (equations III.7, III.8, and III.9). Hence, we ignore these values in Figure 5. This also indicates that the eigenmode solution is not relevant for the range of angles we consider. So, for $0 \leq \theta \leq 40^\circ$, the flux term dominates and the hinge yields a subdominant contribution. This is consistent with our assumption that evaporation drives the fluid flow in the droplet.

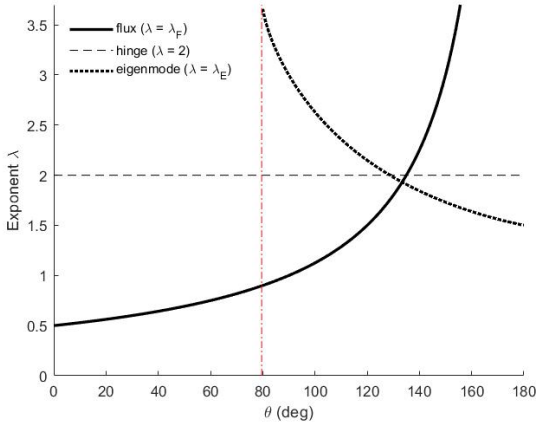

Figure 5: Exponents of the flux, hinge, and eigenmode are plotted in solid, dashed, and dotted lines, respectively. The red vertical line is positioned at $\theta = 79.6^\circ$, below which, the eigenmode solution is not relevant. The dominant contribution is indicated by the smallest exponent. The flux dominates for $\theta < 133.4^\circ$.

In the next three sections, we show plots of the flux, hinge, and eigenmode solutions. We briefly discuss their individual contributions as relevant to this thesis. For further details, we refer interested readers to [13]. The velocities shown in the plots were calculated at polar locations $(\hat{r}, \phi)$, but plotted at the corresponding cartesian coordinates. The x-axis in the plots represents the dimensionless length of the wedge, R_w. Velocity vectors are normalized so they only indicate direction of flow. The velocity is given by the colorbar. All values are dimensionless. We chose $R_w = 1 \times 10^{-5}$, small enough that the dynamics near the contact line can be seen clearly in the plots.

III.5.2 Flux Streamlines

Figure 6 shows the flux solution plotted for $\theta = 15^\circ, 30^\circ,$ and 40°. As anticipated, increased evaporation pulls fluid towards the interface and we see an increase in velocity as the contact line is approached. As discussed earlier, the evaporative flux, equation $III.15$, diverges as $\hat{r} \to 0$ for $\theta < 90^\circ$. Since the velocity yielded by the flux solution is dependent on the evaporative flux, the velocity also diverges for this range of angles as the contact line is approached. We also see the strength of the flow increase as the angle decreases.

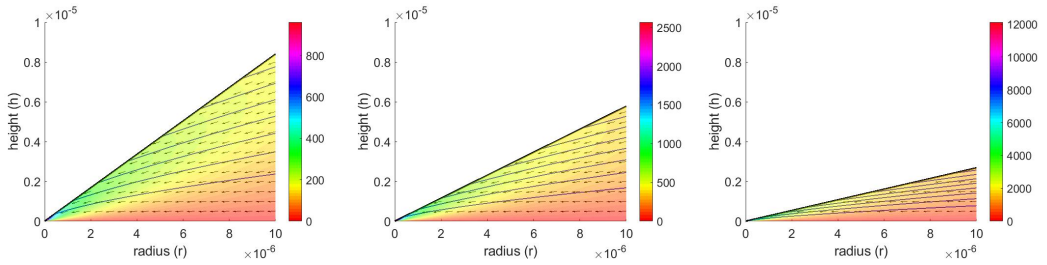

Figure 6: Streamline plots of the flux solution for contact angles (a) $\theta = 40°$, (b) $\theta = 30°$, and (c) $\theta = 15°$. Velocity vectors are normalized and the velocity is given by the colorbar. All values are dimensionless. The length of the wedge is $R_w = 10^{-5}$.

III.5.3 Hinge Streamlines

Figure 7 shows the streamlines for the hinge solution for contact angles $\theta = 15°, 30°,$ and $40°$. The collapsing interface induces a flow away from the contact line, driving fluid towards the center of the drop. There is a competition between the flux and the hinge, which drive fluid in opposite directions. However, the dimensionless velocities in the flux results are on the order of 10^3, while the the fastest dimensionless hinge velocities are on the order of 10^{-4}. Thus, the hinge contribution is negligible compared to the flux contribution for $\theta \leq 40°$. However, in future work, we will consider higher initial contact angles for which the hinge may have a greater contribution to the fluid velocity.

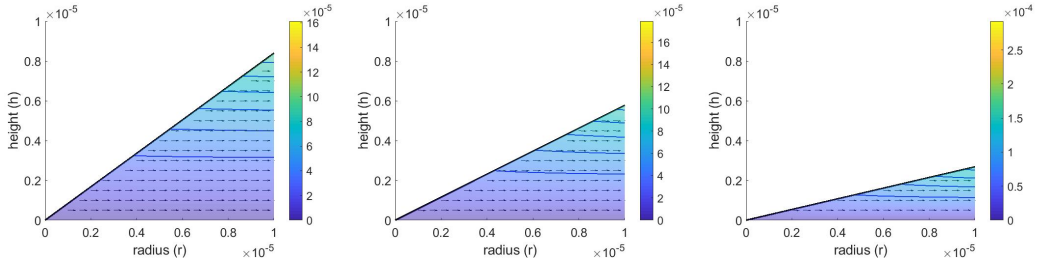

Figure 7: Streamline plots of the hinge solution for contact angles (a) $\theta = 40°$, (b) $\theta = 30°$, and (c) $\theta = 15°$. Velocity vectors are normalized so that they indicate direction only. The velocities are given by the colorbar. All values are dimensionless. The length of the wedge is $R_w = 10^{-5}$.

III.5.4 Eigenmode Streamlines

Recall the eigenmode solution was found up to an unknown constant. Gelderblom et al. claim this constant to be order one, hence, as was done in [13], we let $D_E(\theta) = 1$ to study the contribution of the eigenmode solution. Figure 8 shows plots of the eigenmode streamlines and velocity field for angles $\theta = 15°, 30°,$ and $40°$. In Section III.5.1, we mathematically argued that the eigenmode is irrelevant for our range of angles. The plots provide a physical argument for neglecting the eigenmode. We see in Figure 8 that eddies appear in the flow, circulating fluid in and out of the wedge. This behavior is seen for all angles less than 79.6° [23]. Thus, the net flow into the wedge is zero for this range of angles.

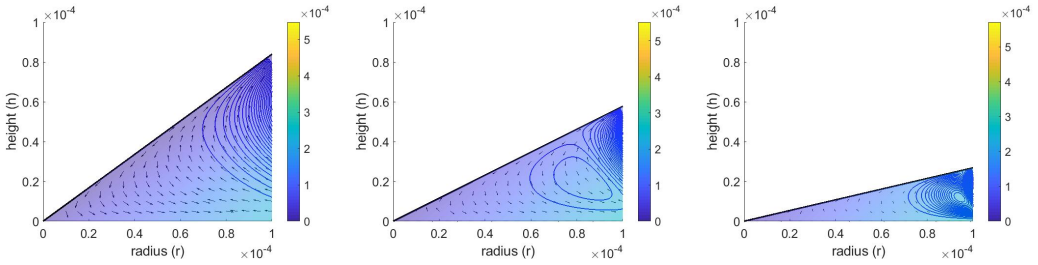

Figure 8: Streamlines from the eigenmode solution for contact angles (a) $\theta = 40°$, (b) $\theta = 30°$, and (c) $\theta = 15°$. Velocity vectors are normalized so that they indicate direction only. The velocities are given by the colorbar. All values are dimensionless. The length of the wedge is $R_w = 10^{-5}$.

III.5.5 Full Solution

The full solution to the stream function is obtained by superposition of equations III.47, III.64, and III.77. Thus, the flow inside of the wedge is characterized by the equation,

$$\psi(\hat{r}, \phi, t) = \frac{J_0(\theta)}{M(\lambda_F, \theta)} \hat{r}^{\lambda_F} f(\phi, \theta) + \frac{\beta(\theta)}{N(\theta)} \hat{r}^2 g(\phi, \theta) + D_E(\theta) \hat{r}^{\lambda_E} h(\phi, \theta) \tag{III.79}$$

However, since the eigenmode contributes nothing to the net flow into the wedge for our range of angles, we let $D_E(\theta) = 0$. Figure 9 shows the velocity field and streamlines for the full solution. As anticipated, the flux dominates. In fact, the velocity field produced by the full solution appears essentially the same as that produced by just the flux solution. We see fluid pulled towards the contact line at increasing velocity, which is of the same order as the flux velocity.

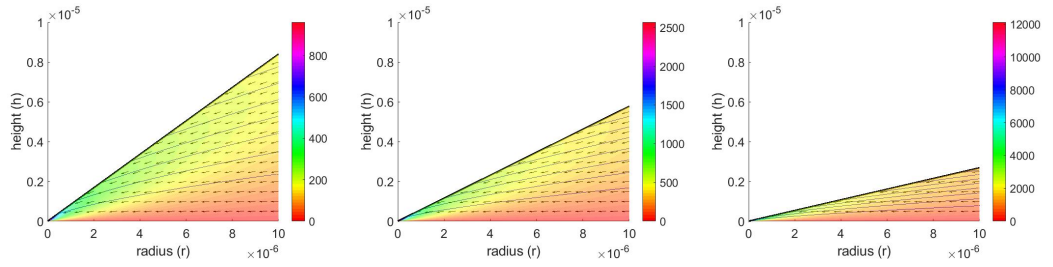

Figure 9: Streamline plots of the full wedge solution for contact angles (a) $\theta = 40°$, (b) $\theta = 30°$, and (c) $\theta = 15°$. Velocity vectors are normalized and the velocity is given by the colorbar. All values are dimensionless. The length of the wedge is $R_w = 10^{-5}$. The unknown constant is $D_E = 0$.

IV. Connecting the Full Drop and Contact Line Regions

IV.1 Boundary Conditions Between Full Drop and Contact Line Regions

To connect the full drop region to the contact line region, we specify a height condition and a volumetric flux condition at the boundary between the two regions. Because we assume the behavior in the vicinity of the contact line drives the flow in the droplet, these conditions are imposed by the wedge. Note all quantities in the following discussion are dimensionless. We introduce the notation $\hat{h}$ to describe the dimensionless height of the interface in the contact line region. Since we model the contact line region as a wedge, the position of the interface can be described in cylindrical coordinates by the equation

$$\hat{h}(r,t) = (1-r)\tan\theta(t), \tag{IV.1}$$

where $1 - R_w \leq r \leq 1$.

To obtain our first boundary condition, we match the dimensional droplet height, $h'(r',t') = \epsilon R' h(r,t)$, to the dimensional wedge height, $h'_w(r'_w,t') = R'\hat{h}(r_w,t)$, at the boundary. That is, $h(1-R_w,t) = \frac{\hat{h}(1-R_w,t)}{\epsilon}$. It follows that $\frac{\partial h}{\partial t}(1-R_w,t) = \frac{1}{\epsilon}\frac{\partial \hat{h}}{\partial t}(1-R_w,t)$. Thus,

$$\frac{\partial h}{\partial t}(1-R_w,t) = \frac{R_w \sec^2\theta}{\epsilon}\frac{\partial \theta}{\partial t}. \tag{IV.2}$$

This condition states that the interface evolution equation at the boundary must match the interface evolution of the wedge.

The second boundary condition states that the volumetric flux across the boundary, $Q(r,t)$, is determined by the volumetric flux in the wedge, $\hat{Q}(\hat{r},t)$. Thus,

$$Q(1-R_w,t) = -\frac{\hat{Q}(R_w \sec\phi, t)}{\epsilon}. \tag{IV.3}$$

Note the scaling with $\frac{1}{\epsilon}$ is a result of the vertical scaling in the lubrication approximation, $z' = \epsilon R' z$.

IV.2 Initial Condition

To solve the evolution equation, we must provide an initial condition. Since we applied lubrication theory in the full drop region, we use an initial condition with constant curvature given by,

$$h(r,0) = a(1-r^2) + b, \tag{IV.4}$$

where a and b are constants. To determine the coefficients of the initial condition, we use the fact that the full drop and wedge heights match at the boundary. Thus,

$$a[1-(1-R_w)^2] + b = \frac{R_w \tan\theta}{\epsilon}. \tag{IV.5}$$

We also enforce that the slope of the initial condition at the boundary match the wedge slope. That is, $\frac{\partial h}{\partial r} = \frac{1}{\epsilon}\frac{\partial \hat{h}}{\partial r}$, which yields the expression

$$-2a(1-R_w) = -\frac{\tan\theta}{\epsilon}, \tag{IV.6}$$

from which it follows that

$$a = \frac{\tan\theta}{2\epsilon(1-R_w)}. \tag{IV.7}$$

Plugging this value for a into equation IV.5, we get,

$$\frac{\tan\theta}{2\epsilon(1-R_w)}[1-(1-R_w)^2]+b=\frac{R_w\tan\theta}{\epsilon}, \tag{IV.8}$$

and solving for b yields,

$$b=\frac{\tan\theta}{2\epsilon}\left(R_w-\frac{1}{1-R_w}+1\right). \tag{IV.9}$$

V. Numerical Methods

We implemented a method of lines to solve the interface evolution equation (II.32) and boundary conditions. All spatial derivatives were approximated using second-order central finite differences. The resulting system of ODEs was solved using ode15s in MATLAB, yielding the height of the interface at each time. We solved over the dimensionless domain $0 \leq r \leq 1-R_w$ using an equally spaced grid with grid spacing Δr.

At each spatial location in our solving scheme, we must know the heights two steps ahead and two steps behind since we are approximating a fourth-order PDE using second-order finite difference approximations. Thus, at $r=0$, $r=\Delta r$, $r=1-R_w-\Delta r$, and $r=1-R_w$, we must apply boundary conditions to obtain the information we need. At $r=0$ and $r=\Delta r$, we take advantage of the symmetry of the droplet. At $r=1-R_w-\Delta r$, instead of expanding the interface evolution equation and discretizing the spatial derivatives, we discretized the volumetric flux term using a second-order central finite difference, and implemented boundary condition IV.3. At $r=1-R_w$, we implemented boundary condition IV.2.

We verified our code using the Method of Manufactured Solutions (MMS), developed by Roache [28], in which we evaluate the error of our numerical solution from a known solution of our choosing. This simply determines whether or not our code produces an expected result, giving no concern for physical reality.

To implement MMS, we neglect the wedge and assume the solution is given by the equation of a spherical cap,

$$h_E(r,t)=\sqrt{\frac{1}{\sin^2\theta(t)}-r^2}-\cot\theta(t) \tag{V.1}$$

where we refer to the exact height as h_E.

We want our numerical height to equal the exact height. That is, we want $h(r,t) = h_E(r,t)$, or, equivalently, $\frac{\partial h}{\partial t} = \frac{\partial h_E}{\partial t}$. The idea behind MMS is to utilize a forcing function such that the time derivatives match. Thus, the new interface evolution equation becomes,

$$\frac{\partial h}{\partial t}(r,t) = -\frac{1}{r}\frac{\partial}{\partial r}(rQ(r,t)) + \frac{\partial h_E}{\partial t} + \frac{1}{r}\frac{\partial}{\partial r}(rQ_E(r,t)), \tag{V.2}$$

where $Q_E(r,t)$ is the volumetric flux in the spherical cap. The last two terms on the right side of equation V.2 make up the forcing function. If the code works properly, then the solution should be an approximation of $h_E(t)$.

We solve over the domain $0 \leq r \leq 1 - R_w$ for an initial contact angle $\theta = 30°$. At the boundary, $r = 1 - R_w$, we let $Q(1 - R_w, t) = Q_E(1 - R_w, t)$. We let $\Delta r = 0.01$ and $\frac{d\theta}{dt} = -\frac{\pi}{6}$ so that the droplet would evaporate in a dimensionless time of one.

Figure 10 shows the absolute error plotted as a function of the radius for several times. The error is small, on the order of 10^{-5}, which is consistent with a second-order accurate scheme, for which we anticipate the error to be no larger than $(\Delta r)^2$.

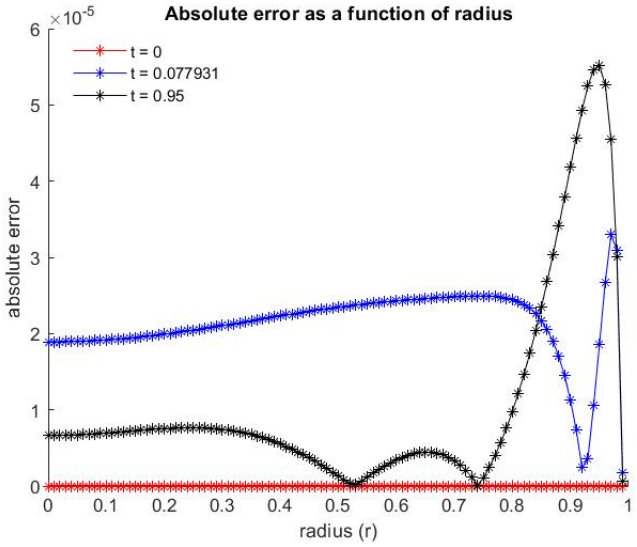

Figure 10: Absolute error plotted as a function of the radius for three different times: at the beginning of the simulation, part way into the simulation, and at the end of the simulation.

VI. Results

Our method for connecting the two regions, outlined in Section IV, relies on the rate at which the wedge interface decreases, $\frac{\partial \hat{h}}{\partial t}$, and the volumetric flow into the wedge, $\hat{Q}$. In turn, each of these depend on the rate at which the angle decreases, $\frac{d\theta}{dt}$, and the evaporative flux in the wedge, $\hat{J}$. Thus, implicitly, the two key parameters upon which our scheme hinges are $\frac{d\theta}{dt}$ and $\hat{J}$. In this section, we study the impact these two factors have on the evolution of the droplet interface. All simulations were run with $R_w = 0.005$, which corresponds to a dimensional value of $R_w' = 5 \times 10^{-6}$ meters, for initial contact angles $\theta = 15^\circ, 30^\circ, 40^\circ$. Note that all plots in this section contain dimensionless values. However, we discuss dimensional results.

Before discussing simulations of the evaporating droplet, we first analyze the evaporative flux and volumetric flux at the boundary. The evaporative flux was calculated using the dimensionless form of equation III.13 and evaluated at $\hat{r} = R_w \sec\theta$, which is the position of the boundary at the interface stated in polar coordinates. To calculate $\hat{Q}$ at the boundary, we integrate the radial velocity, v_r, across the vertical boundary between the full drop and the wedge. We write $v_r(1 - R_w, t)$ in terms of the polar velocities by rotating $u_r(R_w \sec\phi, t)$ and $u_\phi(R_w \sec\phi, t)$. Then the volumetric flux across the boundary is given by,

$$\hat{Q}(R_w \sec\phi, t) = \int_0^h v_r(1 - R_w, t)\, dz = \int_0^\theta [u_r(R_w \sec\phi, t)\cos\phi - u_\phi(R_w \sec\phi, t)\sin\phi] R_w \sec^2\phi\, d\phi. \tag{VI.1}$$

To calculate both $\hat{J}$ and $\hat{Q}$, we used a constant expression for $\frac{d\theta}{dt}$ obtained by fitting a line to data. This is shown in Figure 11. The expression for the rate of contact angle decrease is given by the slope of the dashed line. Thus, dimensionally, $\frac{d\theta}{dt'} = -0.11$ degrees/s. This determines the time is takes for the wedge to evaporate, which we assume sets the time scale for the entire droplet. We note here that the rate of contact angle decrease is not truly linear, as is seen by the solid curve in Figure 11. However, at this stage in our research, we desire simplicity over a rigorous fit. We also recognize that using an expression for $\frac{d\theta}{dt}$ based on particular experiments is not sufficient for linking our two models, as we discuss in more detail later.

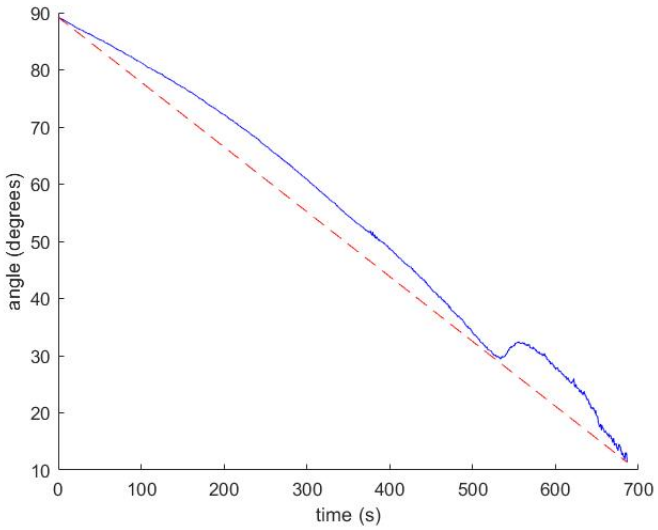

Figure 11: The blue, solid curve shows the angle at each time for a particular experiment performed by the DMFL. The dashed red line shows a linear fit between the first and last data points. In the experiment, the initial contact angle was $\theta = 89^\circ$ and the drying time was approximately 11.52 minutes.

Figure 12 shows both $\hat{J}(R_w \sec\theta, t)$ and $\hat{Q}(R_w \sec\phi, t)$ plotted against time for initial contact angles of $\theta = 15^\circ, 30^\circ,$ and 40°. The arrows indicate direction of decreasing contact angle. For $\theta = 15^\circ$, ode15s has difficulty integrating the interface evolution equation (eq. II.32) forward in time beyond the dimensionless time of $t = 0.024$. Thus, the evaporative and volumetric fluxes are plotted only up to $t = 0.024$. In Figure 12a, we see the evaporative flux increases over time for all angles, as expected. Over the entire drying time, $\hat{J}$ is order unity, which is consistent with prior work [9, 13, 14, 27]. In Figure 12b, we see the volumetric flux increases in magnitude over time. Thus, as the evaporation rate increases, more fluid is sucked out of the full drop, driving a stronger radial flow into the wedge. We also note the volumetric flux has the appropriate sign. Because the contact line region is modeled with the contact line at the origin, negative $\hat{Q}$ indicates flow towards the contact line. We continue with our analysis confident that both the evaporative flux and the volumetric flux are at least exhibiting anticipated behavior.

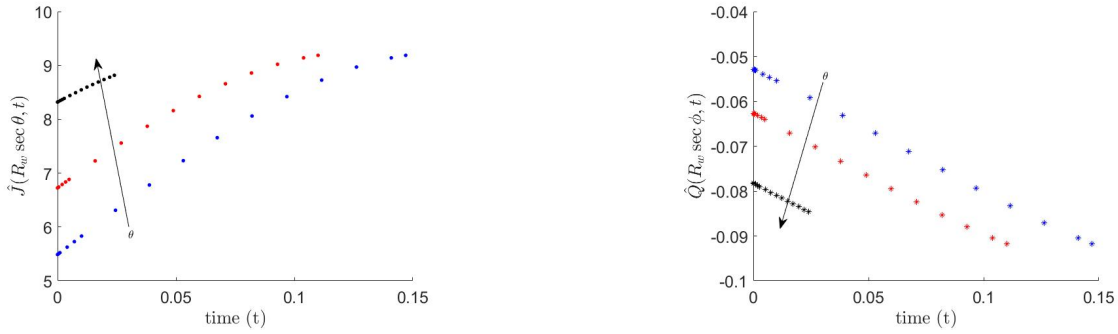

(a) **(b)**

Figure 12: Plots of (a) the evaporative flux at the boundary as a function of time and (b) the volumetric flux at the boundary as a function of time. Both are plotted for contact angles $\theta = 40°, 30°,$ and $15°$. The black arrows indicate the direction of contact angle decrease. All values are dimensionless.

VI.1 Comparison of the Interface Evolution With and Without Evaporation

To begin our analysis of the interface evolution, we shut off evaporation ($J_0 = 0$) and set the volumetric flux at the boundary equal to zero for all time, $\hat{Q}(R_w \sec\theta, t) = 0$. Theoretically, nothing should happen. However, recall we determined $\frac{d\theta}{dt}$ from data; thus, it is decoupled from the evaporative flux expression, and the wedge still evaporates in our simulation since $\frac{d\theta}{dt} \neq 0$. In other words, our expression for $\frac{d\theta}{dt}$ does not know that evaporation has been shut off. Since the wedge interface still comes down and we turned off both methods by which fluid is transferred out of the full drop, we observe a slight increase of the interface towards the center of the drop as fluid is pushed towards the droplet center (Figures 13a, 13c, 13e). This first simulation indicates not much happens without evaporation, which gives us some confidence that our code properly captures the assumption that evaporation in the contact line region drives the motion of the interface. We then turned on evaporation and set the volumetric flux at the boundary equal to the volumetric flux in the wedge (Figures 13b, 13d, 13f). Figure 13 shows results of our first two simulations. The dimensionless height of the interface is plotted in each figure over the domain $0 \leq r \leq 1 - R_w$, which corresponds to a dimensional domain of $0 \leq r' \leq 9.95 \times 10^{-4}$ meters. Arrows indicate direction of interface movement over time. Clearly, turning on evaporation drives the interface down. In fact, the full drop fully evaporates before the wedge does, indicating that the two models do not evaporate on the same time scale. We can correct this by either scaling back evaporation or adjusting the time scale of the wedge. We consider both these scenarios in the next two sections, but before doing so, we discuss some dimensional results.

In Figure 13b, $\theta = 40^\circ$ is the initial contact angle, $h(0,0) = 243.25$ is the initial center height, and $t_f \approx 0.15$. To obtain the dimensional center height, $h'(0,0)$, we multiplied $h(0,0)$ by $\epsilon R'$ and to obtain the dimensional time, t'_f, we multiplied t_f by our time scale $\frac{R'}{V'}$, which was chosen based on the vapor diffusion. The dimensional center height is $h'(0,0) \approx 4.22 \times 10^{-4}$ meters, which is comparable to the observed height of $h'(0,0) \approx 2.6 \times 10^{-4}$ meters. It takes the wedge $t'_f \approx 5.85$ minutes to evaporate with curves plotted at intervals of 1.17 minutes. This is slightly faster than the observed drying time for $\theta = 40^\circ$, $t'_f \approx 6.08$ minutes. Recall the evaporative flux and volumetric flux from Figure 12. To obtain these values in dimensions, we multiplied $\hat{J}$ by the density of water, ρ, and the velocity scale, V', and $\hat{Q}$ by $V'R'$. The evaporative flux varies approximately over time from $2.3 \times 10^{-3} \frac{\text{kg}}{\text{m}^2\text{s}}$ to $3.8 \times 10^{-3} \frac{\text{kg}}{\text{m}^2\text{s}}$ while volumetric flux varies approximately over time from $-2.23 \times 10^{-11} \frac{\text{m}^3}{\text{s}}$ to $-3.84 \times 10^{-11} \frac{\text{m}^3}{\text{s}}$.

In Figure 13d, $\theta = 30^\circ$ is the initial contact angle with $h(0,0) = 167.08$ and $t_f \approx 0.11$, corresponding to dimensional values $h'(0,0) = 2.90 \times 10^{-4}$ meters and $t'_f = 4.38$ minutes with curves plotted at intervals of 0.88 minutes. The evaporative flux varies approximately over time from $2.8 \times 10^{-3} \frac{\text{kg}}{\text{m}^2\text{s}}$ to $3.8 \times 10^{-3} \frac{\text{kg}}{\text{m}^2\text{s}}$ while the volumetric flux varies approximately over time from $-2.64 \times 10^{-11} \frac{\text{m}^3}{\text{s}}$ to $-3.85 \times 10^{-11} \frac{\text{m}^3}{\text{s}}$.

In Figure 13f, $\theta = 15^\circ$ is the initial contact angle with $h(0,0) = 77.54$ and $t_f \approx 0.055$, corresponding to dimensional values $h'(0,0) = 1.35 \times 10^{-4}$ meters and $t'_f \approx 2.19$ minutes. However, as previously mentioned, we were unable to run our code for the entire evaporation time. The initial evaporative flux is approximately $3.5 \times 10^{-3} \frac{\text{kg}}{\text{m}^2\text{s}}$ while the initial volumetric flux is approximately $-3.29 \times 10^{-11} \frac{\text{m}^3}{\text{s}}$.

To give a better idea of what's happening at the boundary, Figure 14b shows a blown-up image of the boxed region in Figure 14a, in which the initial contact angle is $\theta = 30^\circ$. The dashed vertical line indicates the boundary between the droplet region and the contact line region. For almost half the drying time, the slope of the droplet actually matches the slope of the wedge reasonably well, but then we begin to see the droplet flattening more quickly than the wedge.

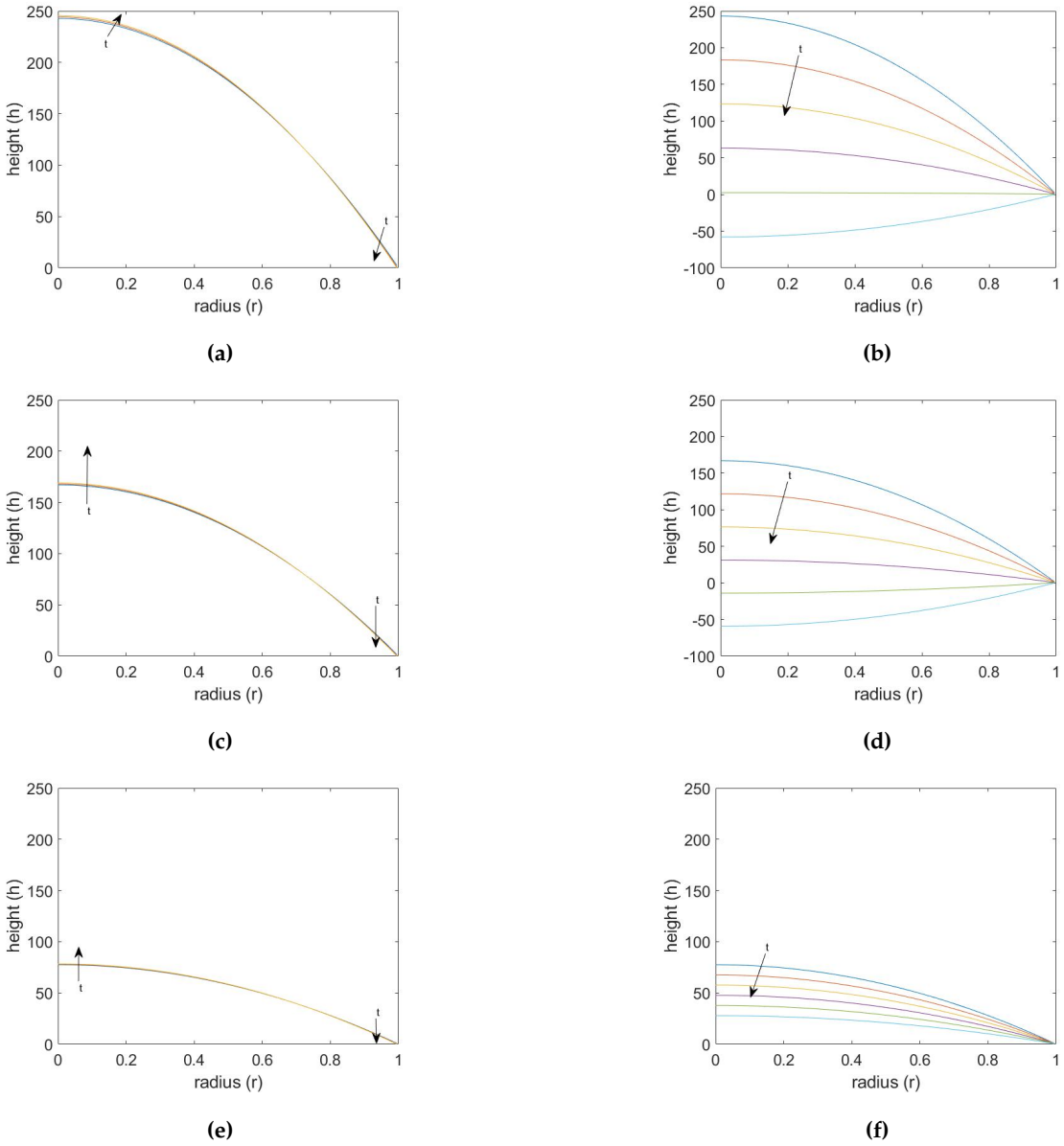

Figure 13: Plot (a) $\theta = 40^\circ$ with no evaporation; (b) $\theta = 40^\circ$ with evaporation; (c) $\theta = 30^\circ$ with no evaporation; (d) $\theta = 30^\circ$ with evaporation; (e) $\theta = 15^\circ$ with no evaporation; (f) $\theta = 15^\circ$ with evaporation run to dimensionless time of $t = 0.024$. Both axes contain dimensionless values. The black arrows indicate the direction of interface movement over time.

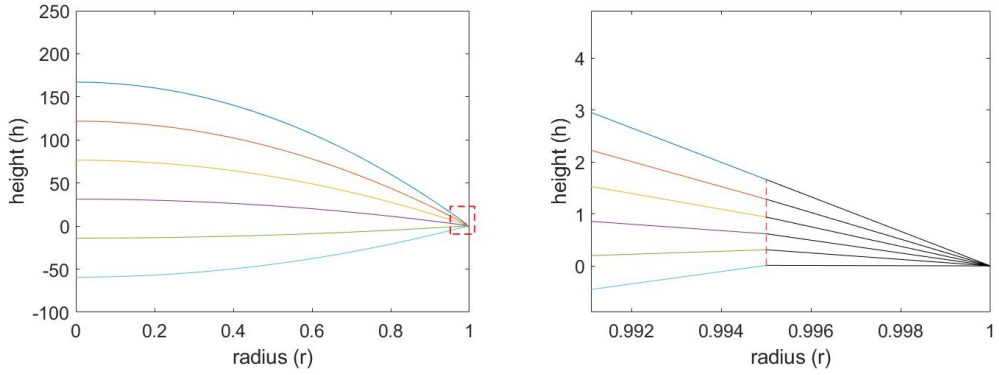

(a) **(b)**

Figure 14: Zoomed in view of the contact line region (boxed area) when the interface evolution is simulated with evaporation on for an initial contact angle of $\theta = 30°$. The dashed vertical line indicates the location of the boundary between the full drop region and the contact line region. Axes values are dimensionless.

VI.2 Effects of Adjusting Evaporative Flux

Clearly, the full drop and the wedge do not evaporate within the same time frame. In this section, we keep the time scale the same as in our previous simulations and adjust the coefficient of the evaporative flux expression until the full drop and the wedge evaporate within the same time frame. Figure 15 shows results of this scenario. The interface is plotted as a function of the radius for several times. The evaporative and volumetric fluxes are plotted over the evaporation time.

Figures 15a, 15b, and 15c show the interface evolution, the evaporative flux, and the volumetric flux, respectively, for an initial contact angle of 40°. In order for the full drop interface to decrease on the wedge time scale, the evaporative flux was scaled by a factor of 0.82, resulting in approximate dimensional values of $1.9 \times 10^{-3} \frac{\text{kg}}{\text{m}^2\text{s}}$ to $3.2 \times 10^{-3} \frac{\text{kg}}{\text{m}^2\text{s}}$ for the evaporative flux and $-1.83 \times 10^{-11} \frac{\text{m}^3}{\text{s}}$ to $-3.16 \times 10^{-11} \frac{\text{m}^3}{\text{s}}$ for the volumetric flux.

Figures 15d, 15e, and 15f show the interface evolution, the evaporative flux, and the volumetric flux, respectively, for an initial contact angle of 30°. In order for the full drop interface to decrease on the wedge time scale, the evaporative flux was scaled by a factor of 0.74, resulting in approximate dimensional values of $2.1 \times 10^{-3} \frac{\text{kg}}{\text{m}^2\text{s}}$ to $2.8 \times 10^{-3} \frac{\text{kg}}{\text{m}^2\text{s}}$ for the evaporative flux and $-1.94 \times 10^{-11} \frac{\text{m}^3}{\text{s}}$ to $-2.85 \times 10^{-11} \frac{\text{m}^3}{\text{s}}$ for the volumetric flux.

Figures 15g, 15h, and 15i show the interface evolution, the evaporative flux, and the volumetric flux, respectively, for an initial contact angle of 15°. We scaled the evaporative flux expression by a factor of 0.54, which was the largest value we could scale by and still be able to run the code for the entire evaporation time. However, the evaporation was not large enough for the full drop to evaporate with the wedge. Though we show the simulated fluxes, note they are inaccurate and we cannot determine how large the evaporative flux needs to be for the droplet to evaporate.

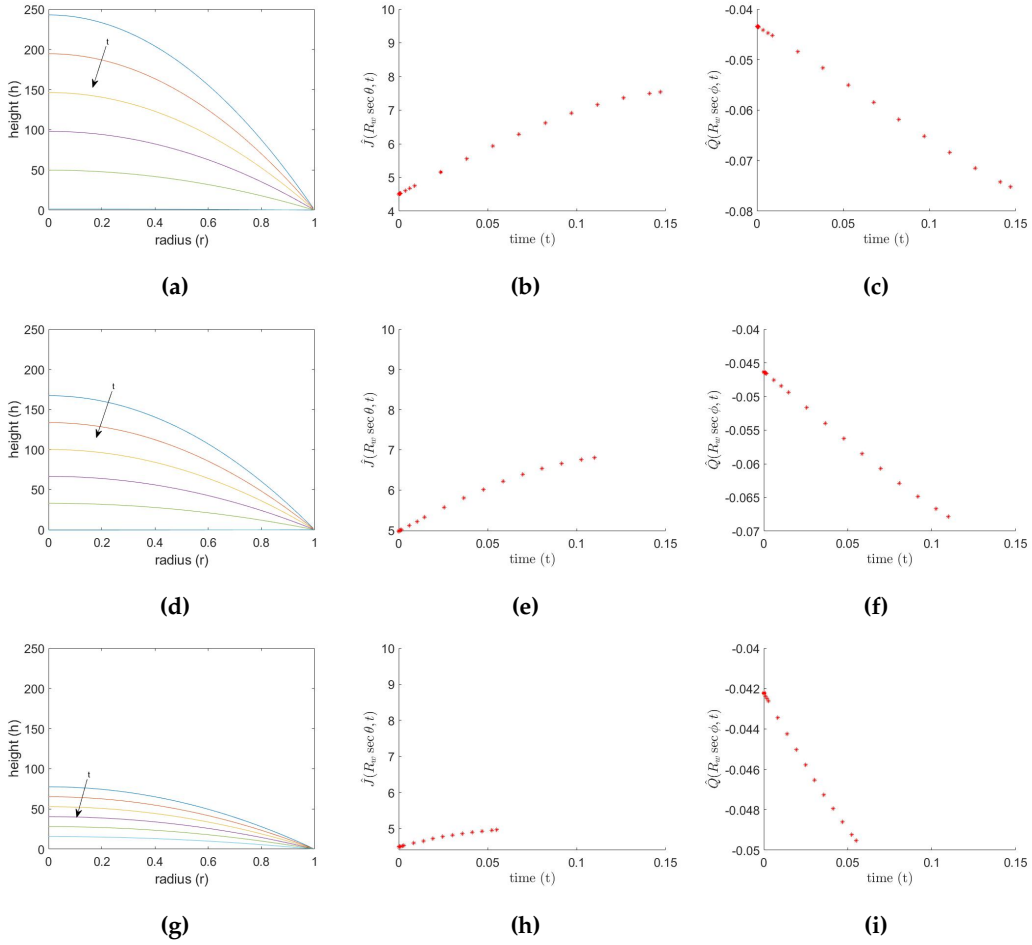

Figure 15: Results of scaling down the evaporative flux. Plots (a), (b), and (c) show the interface evolution, evaporative flux, and volumetric flux for $\theta = 40°$. Plots (d), (e), and (f) show the interface evolution, evaporative flux, and volumetric flux for $\theta = 30°$. Plots (g), (h), and (i) show the interface evolution, evaporative flux, and volumetric flux for $\theta = 15°$. Axes values are dimensionless and are the same for corresponding plots for easier comparison. The black arrows indicate direction of interface movement over time.

In Figure 16b, the boxed region in Figure 16a is blown up to give a better idea of what's happening at the boundary. The dashed vertical line indicates the location of the boundary. The slopes at the boundary now match. Note that we extended the wedge interface into the full drop to show that for some distance beyond the boundary, the slopes still match reasonably well.

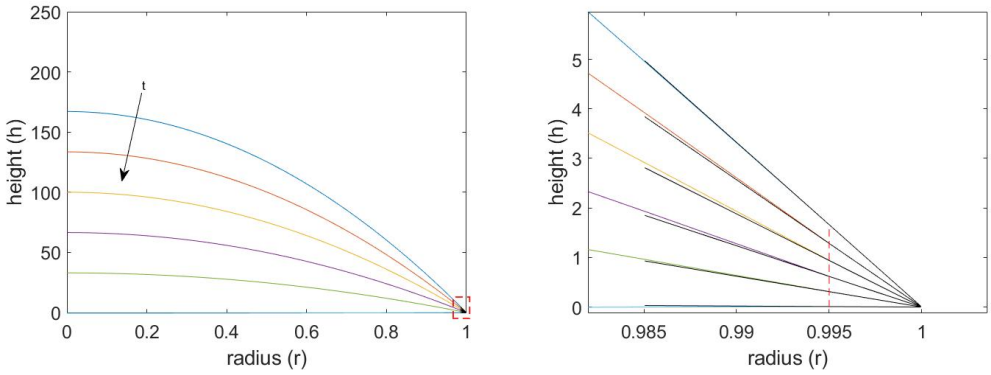

(a) **(b)**

Figure 16: Zoomed in view of the contact line region (boxed area) when the interface evolution is simulated with reduced evaporation for an initial contact angle of $\theta = 30°$. The dashed vertical line indicates the location of the boundary between the full drop region and the contact line region. Axes values are dimensionless. The black arrows indicate direction of interface movement over time.

VI.3 Effects of Adjusting Rate of Contact Angle Decrease

Another means by which we could get the full drop to evaporate within the same time frame as the wedge is to change the wedge time scale. To explore different time scales, we left the evaporative flux alone (the values are the same as reported in Section VI.1) and adjusted the scale of $\frac{d\theta}{dt}$ such that the wedge evaporated faster than in our previous simulations. Figure 17 shows the interface evolution, evaporative flux, and volumetric flux on adjusted time scales for initial contact angles of $\theta = 40°, 30°,$ and $15°$. The interface curves are plotted against the radius for several times. The fluxes are plotted against time. For corresponding plots, the axis limits are the same for easier comparison.

Figures 17a, 17b, 17c show the interface evolution, evaporative flux, and volumetric flux, respectively, for $\theta = 40°$. We sped up the rate of angle decrease by scaling $\frac{d\theta}{dt}$ by a factor of 1.22, which yielded $\frac{d\theta}{dt} \approx -5.77$. The final time was $t_f \approx 0.12$, which translates to an evaporation time of $t'_f \approx 4.81$ minutes, which is about a minute faster than in earlier simulations. Because the volumet-

ric flux depends on $\frac{d\theta}{dt}$ as well as on $\hat{J}$, it changes due to the increased scale on $\frac{d\theta}{dt}$. The dimensional volumetric flux ranges from approximately $-2.22 \times 10^{-11} \frac{\text{m}^3}{\text{s}}$ to $-3.85 \times 10^{-11} \frac{\text{m}^3}{\text{s}}$.

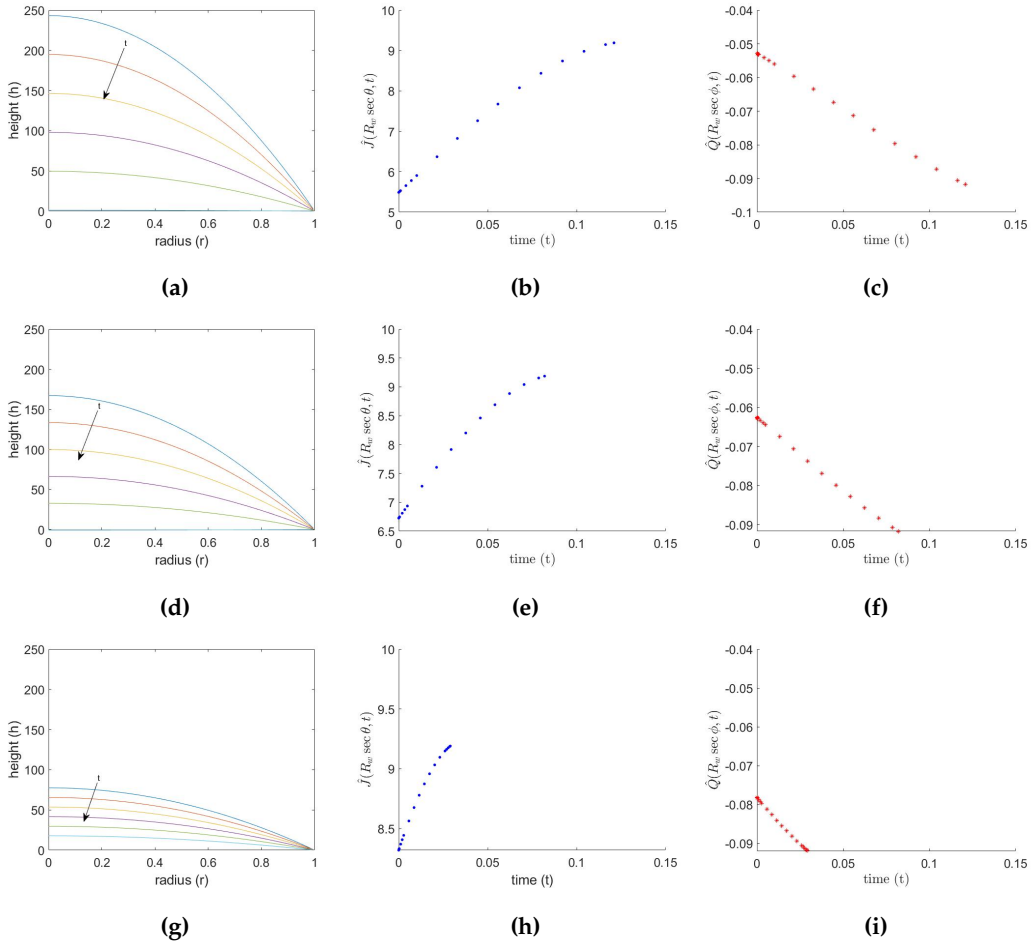

Figure 17: Results of scaling up the rate of angle decrease, which shortens the drying time of the wedge. Plots (a), (b), and (c) show the interface evolution, evaporative flux, and volumetric flux for $\theta = 40°$. Plots (d), (e), and (f) show the interface evolution, evaporative flux, and volumetric flux for $\theta = 30°$. Plots (g), (h), and (i) show the interface evolution, evaporative flux, and volumetric flux for $\theta = 15°$. Axes values are dimensionless and are the same for corresponding plots for easier comparison. The black arrows indicate direction of interface movement over time.

Figures 17d, 17e, 17f show the interface evolution, evaporative flux, and volumetric flux, respectively, for $\theta = 30°$. The rate of angle decrease was scaled by a factor of 1.34, yielding $\frac{d\theta}{dt} \approx -6.33$, and making the final time $t_f \approx 0.08$, or $t'_f \approx 3.26$ minutes. The dimensional volumetric flux ranges from approximately $-3.30 \times 10^{-11} \frac{\text{m}^3}{\text{s}}$ to $-3.87 \times 10^{-11} \frac{\text{m}^3}{\text{s}}$.

Figures 17g, 17h, 17i show the interface evolution, evaporative flux, and volumetric flux, respectively, for $\theta = 15°$. Results for this angle are again questionable since the code has a hard time solving beyond $t_f = 0.024$. We pushed it as far we could, scaling $\frac{d\theta}{dt}$ by 1.9 so that $\frac{d\theta}{dt} \approx -8.98$. The code ran until $t_f \approx 0.029$, or $t'_f \approx 1.15$ minutes. However, this was not long enough for the droplet to evaporate. The resulting volumetric flux ranges from approximately $-2.61 \times 10^{-11} \frac{\text{m}^3}{\text{s}}$ to $-3.85 \times 10^{-11} \frac{\text{m}^3}{\text{s}}$.

Figure 18b shows the blown-up boxed region of Figure 18a. The contact angle is $\theta = 30°$. The dashed vertical line indicates the location of the boundary. As in Figure 16b, the slopes match nicely at the boundary and reasonably well for a distance into the full drop.

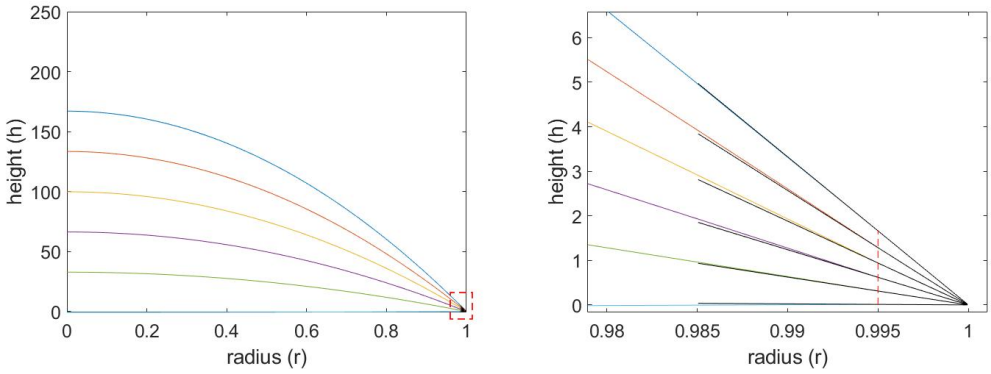

(a) **(b)**

Figure 18: Zoomed in view of the contact line region (boxed area) when the interface evolution is simulated for faster evaporation times in the wedge. The initial contact angle is $\theta = 30°$. The dashed vertical line indicates the location of the boundary between the full drop region and the contact line region. Axes values are dimensionless.

VII. Discussion

VII.1 Discussion and Conclusion

The broad goal of this project was to explore a possible method for capturing the fluid dynamics of an evaporating droplet with a pinned contact line using lubrication theory. We demonstrated the use of a wedge to model the contact line region, building off the work done by Gelderblom and coworkers in [13]. Our more specific research goal was to explore the sufficiency of specifying height and flux conditions at the boundary between the full drop region and the contact line

region. We approximated the rate at which the angle decreases (which sets the time scale for our problem) as a constant value based on data from the DMFL at RIT.

Though our method for connecting the two models appears to be crude, we were still able to show the two pieces can communicate and that connecting a wedge to a lubrication model seems a plausible means of avoiding the breakdown of lubrication theory at a pinned contact line as discussed by Maki and Kumar [21]. Thus, our work at this initial stage gives us reason to pursue further research in this area. Though we do believe it possible for the wedge and lubrication model to communicate, our first attempt at connecting the two pieces by specifying height and flux conditions at the boundary does not appear to be robust enough. We believe it is necessary to explore other means of connecting the droplet region and the contact line region, for reasons we discuss below.

We demonstrated that for an evaporative flux expression as suggested by [9, 13, 14, 15, 27] and a constant $\frac{d\theta}{dt}$ as approximated using data from the DMFL, the droplet interface and the wedge interface do not decrease on the same time scale. We further demonstrated that it is possible for the two interfaces to evaporate simultaneously if we adjust either the evaporative flux or the rate of contact angle decrease. Because several other researchers have successfully used expression III.13, we are inclined to believe this expression should not be adjusted, which brings us to $\frac{d\theta}{dt}$. For much of this project, we were using the expression for $\frac{d\theta}{dt}$ based on the spherical cap assumption, which Gelderblom and coworkers used in [13]. There were two drawbacks to using this expression: (i) we did not necessarily want to assume a spherical cap for all time and (ii) it involves special functions. Earlier in our research progress, we faced difficulty in getting the interface to collapse. We were uncertain how much the complexity of $\frac{d\theta}{dt}$ contributed to our problems. We also attempted to derive our own expression for $\frac{d\theta}{dt}$ following a similar process as outlined by Popov in [27]. In our derivation, we incorporated the wedge geometry and accounted for lubrication theory in the full drop. Our derivation yielded an equation in the form $F_1(\phi)\frac{d\theta}{dt} = F_2(\phi)$, where $F_1(\phi)$ and $F_2(\phi)$ were both very close to zero. Thus, our derivation provided no new information. We show our derivation in the appendix. After our unsuccessful attempt to find our own expression for the rate of angle decrease, we determined it was best to use the simplest possible $\frac{d\theta}{dt}$ for now. Thus, we used data from the DMFL to approximate a constant rate of decrease. However, the results we showed earlier of scaling $\frac{d\theta}{dt}$ reveal faster rates of increase for smaller contact angles, which fits with the stronger evaporation we observe for smaller angles. This indicates that fitting the data with a nonlinear curve may produce better results. That being said, it is concerning that we had to manually adjust factors for different contact angles. The droplet interface did not appear

to automatically adjust to the wedge dynamics. The numerical issues that arise for small contact angles are also of concern.

VII.2 Future Work

We desire to produce a model in which, once the initial angle is set, the full drop automatically adjusts to the behavior of the wedge. We believe a stronger link between the two is necessary to accomplish this. With our current boundary conditions, the wedge dynamics only impact the full drop right at the boundary. In future research, we will investigate adding an additional boundary condition in which we specify the slope, forcing the full drop to match the slant of the wedge interface for all times.

At this initial stage of our research, assuming a known $\frac{d\theta}{dt}$ based on data was sufficient enough to answer our first research question. However, using an expression based on a specific data set limits certain parameters. For example, if we wanted to run simulations for different size droplets, we would likely have to manually adjust $\frac{d\theta}{dt}$ as well. In order to make our model more accurate and versatile, it is of interest to explore use of an implicit relationship between the full drop interface height and the contact angle. This would result in a coupled model in which the full drop piece and the wedge piece feed each other information to simultaneously solve for the interface height and the contact angle. Our proposed additional boundary condition where we specify the slope at the boundary will provide the additional condition to fully couple the models.

The method explored in this project posed significant numerical issues. In each scenario explored in Section VI, our code had difficulty for initial contact angle $\theta = 15^\circ$. We believe this was due, in part, to error build-up in the calculation of $\frac{\partial h}{\partial t}$. Recall we applied lubrication theory to our system of equations to obtain the interface evolution equation. Thus, to match the heights at the boundary, we had to scale the wedge height by $\frac{1}{\epsilon}$, which resulted in a dimensionless initial condition much greater than order one. This lead to an amplified error associated with our spatial discretizations. To reduce error build-up in future work, we will use a spectral method to approximate the spatial derivatives of the height rather than a finite difference method.

VIII. Acknowledgments

I'd like to thank my advisor, Dr. Kara Maki, for her patient guidance and encouragement on this project, for enthusiastic and insightful discussions, and for all the baby clothes. I'd like to thank my committee members, Dr. Steven Weinstein, Dr. Michael Schertzer, and Dr. Nate Barlow, for their encouragement, valuable insights, and interest in this project. Thank you to my family and friends for supporting me in my academic pursuits and for putting up with my attitude when stress overtakes me. Thank you especially to those who've helped me with childcare! Thanks to my parents, John and Jane O'Brien, my sisters Jackie O'Brien and Jen Vrooman, my awesome friends Amy Young and Havilah Tyler, and the most incredible babysitter, Lee Hickey, for being part of my childcare team. I would not have been able to do this without you! Lastly, thank you to my little girl, Anika Rani, for bringing joy and smiles to each day and giving me motivation to keep pushing myself.

This material is based upon work supported by the ADVANCE RIT grant which is funded through the National Science Foundation under Award No. HRD-1209115.

IX. Appendix

IX.1 Rate of Contact Angle Decrease Over Time

An expression for $\frac{d\theta}{dt}$ was derived by Popov in [27] by equating two different arguments for the change in volume. The first argument is based on the fact that volume is lost through evaporation at the surface of the drop, which is represented as the integral of the evaporative flux times the arclength rotated about the center of the drop:

$$\frac{dV'}{dt'} = -\int_0^{R'} \frac{J'(r',t')}{\rho}\sqrt{1+\left(\frac{\partial h'}{\partial r'}\right)^2}\, 2\pi r'\, dr'. \tag{IX.1}$$

The second argument comes from the knowledge that the volume inside the drop can be found by integrating the height rotated about the center of the drop:

$$V' = \int_0^{R'} h'(r',t') 2\pi r'\, dr' \tag{IX.2}$$

.

Taking the time derivative of equation IX.2 yields an expression for the change in volume that contains $\frac{d\theta}{dt'}$. Setting this expression equal to equation IX.1, one can solve for $\frac{d\theta}{dt'}$. Instead of utilizing the derivation in [27], we used a similar approach to derive our own expression for the differential equation of the angle. We chose to do this because, in his derivation, Popov assumes $J'(r',t')$ to be the exact equation found by solving for the vapor concentration. We argue the approximate evaporative flux should be used for consistency. He also assumes $h'(r',t')$ to be a spherical cap for all time. Though we assume the height of our drop to initially be a spherical cap, we do not wish to assume it will remain so. The last reason we derive our own expression is because we approximate the contact line region as a wedge. Our derivation is as follows:

We know the volume in the full drop is given by $2\pi \int_0^{R'-R'_w} h'(r',t') r'\, dr'$ in cylindrical coordinates (r',z') and the volume in the wedge is given by $\pi {R'_w}^2 (R'-R'_w)\tan\theta(t')$ in polar coordinates $(\hat{r}',\phi)$. Therefore, the change in volume over time in the entire droplet is,

$$\frac{dV'}{dt'} = 2\pi \int_0^{R'-R'_w} \frac{\partial h'(r',t')}{\partial t'} r'\, dr' + \pi {R'_w}^2 (R'-R'_w)\sec^2\theta(t')\frac{d\theta}{dt'} \tag{IX.3}$$

We know the time derivative in the full drop is given by,

$$\frac{\partial h'}{\partial t'} = -\frac{1}{r'}\frac{\partial}{\partial r'}(r'Q') - \frac{J'(r',t')}{\rho} \tag{IX.4}$$

Plugging equation IX.4 into equation IX.3, we obtain,

$$\frac{dV'}{dt'} = 2\pi \int_0^{R'-R'_w} - \left(\frac{1}{r'}\frac{\partial}{\partial r'}(r'Q') - \frac{J'(r',t')}{\rho}\right) r'\, dr' + \pi {R'_w}^2 (R' - R'_w)\sec^2\theta(t')\frac{d\theta}{dt'} \tag{IX.5}$$

Note the integral in equation IX.5 can be split and rewritten as

$$2\pi\left(-r'Q'\Big|_0^{R'-R'_w} - \int_0^{R'-R'_w} \frac{J'(r',t')}{\rho}\, dr'\right) = -2\pi(R'-R'_w)Q'(R'-R'_w,t') - 2\pi\int_0^{R'-R'_w}\frac{J'(r',t')}{\rho}r'\, dr' \tag{IX.6}$$

Further note that $Q'(R'-R'_w,t')$ is the volumetric flux at the boundary between the full drop and the wedge. Then $Q'(R'-R'_w,t') = \hat{Q}'(R'_w\sec\phi,t')$, where $\hat{Q}'$ is the volumetric flux in the wedge and $\hat{r}'(\phi) = R'_w\sec\phi$ is the polar radius as a function of the angle. Then equation IX.5 can be expressed as,

$$\frac{dV'}{dt'} = -2\pi(R'-R'_w)\hat{Q}'(R'_w\sec\phi,t') - 2\pi\int_0^{R'-R'_w}\frac{J'(r',t')}{\rho}r'\, dr' + \pi {R'_w}^2(R'-R'_w)\sec^2\theta(t')\frac{d\theta}{dt'}. \tag{IX.7}$$

To get a second expression for the change in volume, we modify equation IX.1 to incorporate the wedge:

$$\frac{dV'}{dt'} = -2\pi\int_0^{R'-R'_w}\frac{J'(r',t')}{\rho}r'\, dr' - 2\pi(R'-R'_w)\int_0^{R'_w sec\theta}\frac{J'(\hat{r}',t')}{\rho}\, d\hat{r}' \tag{IX.8}$$

The first integral in equation IX.8 describes the change in volume in the full drop, which was simplified by noting $\sqrt{1+\left(\frac{\partial h'}{\partial r'}\right)^2} \approx 1$ in lubrication theory. The second integral describes the change in volume in the wedge and is written in polar coordinates, $(\hat{r}',\phi)$.

We now have arrived at two different expressions for $\frac{dV'}{dt'}$. Setting equation IX.7 equal to IX.8 and simplifying, we get,

$$\hat{Q}'(R'_w\sec\phi,t') - \frac{{R'_w}^2\sec^2\theta(t')}{2}\frac{d\theta}{dt'} = \int_0^{R'_w\sec\theta}\frac{J'(\hat{r}',t')}{\rho}\, d\hat{r}'. \tag{IX.9}$$

The volumetric flux in the wedge depends on the rate at which the contact angle decreases. Hence, to isolate $\frac{d\theta}{dt'}$, we must first rewrite $\hat{Q}'$ in terms of $\frac{d\theta}{dt'}$. To obtain $\hat{Q}'$, we integrate the velocity of the horizontal flow, $v_r'(r', t')$, across the boundary between the full drop and the wedge. Since the horizontal velocity is in cylindrical coordinates, we rotate the polar velocities $u_{\hat{r}'}'(\hat{r}', t')$ and $u_{\phi}'(\hat{r}', t')$. Then the volumetric flow across the boundary is given by,

$$\hat{Q}'(R_w' \sec\phi, t') = \int_0^{R_w' \tan\theta} v_r'(R' - R_w', t')\, dy' = \int_0^{\theta} [u_{\hat{r}'}'(R_w' \sec\phi, t')\cos\phi - u_{\phi}'(R_w' \sec\phi, t')\sin\phi](R_w' \sec^2\phi)\, d\phi \tag{IX.10}$$

The velocities are comprised of a contribution from the flux solution and one from the hinge solution. So we can rewrite equation IX.10 as,

$$\hat{Q}'(R_w' \sec\phi, t') = \int_0^{\theta} [(u'^F_{\hat{r}} + u'^H_{\hat{r}'})\cos\phi - (u'^F_{\phi} + u'^H_{\phi})\sin\phi](R_w' \sec^2\phi)\, d\phi, \tag{IX.11}$$

where the velocities are evaluated at $\hat{r}' = R_w' \sec\phi$. Splitting up the integral, we get,

$$\begin{aligned}\hat{Q}'(R_w' \sec\phi, t') = {} & R_w' \int_0^{\theta} u'^F_{\hat{r}'} \sec\phi\, d\phi + R_w' \int_0^{\theta} u'^H_{\hat{r}'} \sec\phi\, d\phi \\ & - R_w' \int_0^{\theta} u'^F_{\phi} \sin\phi \sec^2\phi\, d\phi - R_w' \int_0^{\theta} u'^H_{\phi} \sin\phi \sec^2\phi\, d\phi.\end{aligned} \tag{IX.12}$$

Substituting equation IX.12 into equation IX.9 and dividing by R_w yields,

$$\int_0^{\theta} u'^F_{\hat{r}'} \sec\phi\, d\phi + \int_0^{\theta} u'^H_{\hat{r}'} \sec\phi\, d\phi - \int_0^{\theta} u'^F_{\phi} \sin\phi \sec^2\phi\, d\phi - \int_0^{\theta} u'^H_{\phi} \sin\phi \sec^2\phi\, d\phi - \frac{R_w' \sec^2\theta(t')}{2}\frac{d\theta}{dt'} = \frac{1}{R_w'}\int_0^{R_w' \sec\theta} \frac{J'(\hat{r}', t')}{\rho}\, d\hat{r}'. \tag{IX.13}$$

Recall we wish to isolate $\frac{d\theta}{dt'}$, which is contained in the hinge pieces. Hence, we move the flux integrals to the other side of equation IX.13:

$$\begin{aligned}&\int_0^{\theta} u'^H_{\hat{r}'} \sec\phi\, d\phi - \int_0^{\theta} u'^H_{\phi} \sin\phi \sec^2\phi\, d\phi - \frac{R_w' \sec^2\theta(t')}{2}\frac{d\theta}{dt'} = \\ &- \int_0^{\theta} u'^F_{\hat{r}'} \sec\phi\, d\phi + \int_0^{\theta} u'^F_{\phi} \sin\phi \sec^2\phi\, d\phi + \frac{1}{R_w'}\int_0^{R_w' \sec\theta} \frac{J'(\hat{r}', t')}{\rho}\, d\hat{r}'.\end{aligned} \tag{IX.14}$$

Recall the velocities, $u'_{\hat{r}'}$ and u'_{ϕ}, in equation III.4 and the hinge solution, ψ_H, in equation III.64. Substituting equation III.64 into the velocity expressions in equation III.4, we find,

$$u'^{H}_{\hat{r}'}(R'_w \sec\phi, t') = \frac{R'_w \sec\phi}{N(\theta)} \frac{d\theta}{dt'} K(\phi, \theta) \tag{IX.15}$$

where

$$K(\phi, \theta) = 2\cos(2\phi) + 2\tan(2\theta)\sin(2\phi) - 2 \tag{IX.16}$$

and

$$u'^{H}_{\phi}(R'_w \sec\phi, t') = -\frac{2(R'_w \sec\phi)}{N(\theta)} \frac{d\theta}{dt'} k(\phi, \theta) \tag{IX.17}$$

where

$$k(\phi, \theta) = \sin(2\phi) - \tan(2\theta)\cos(2\phi) - 2\phi + \tan(2\theta). \tag{IX.18}$$

We can rewrite equation IX.14 as,

$$\begin{aligned} \frac{R'_w}{N(\theta)} \frac{d\theta}{dt'} \int_0^{\theta} K(\phi, \theta) \sec^2\phi \, d\phi + \frac{2R'_w}{N(\theta)} \frac{d\theta}{dt'} \int_0^{\theta} k(\phi, \theta) \sin\phi \sec^3\phi \, d\phi - \frac{R'_w \sec^2\theta(t')}{2} \frac{d\theta}{dt'} \\ = -\int_0^{\theta} u'^{F}_{\hat{r}'} \sec\phi \, d\phi + \int_0^{\theta} u'^{F}_{\phi} \sin\phi \sec^2\phi \, d\phi + \frac{1}{R'_w} \int_0^{R'_w \sec\theta} \frac{J'(\hat{r}', t')}{\rho} \, d\hat{r}'. \end{aligned} \tag{IX.19}$$

Solving for $\frac{d\theta}{dt'}$,

$$\frac{d\theta}{dt'} = \frac{-\int_0^{\theta} u'^{F}_{\hat{r}'} \sec\phi \, d\phi + \int_0^{\theta} u'^{F}_{\phi} \sin\phi \sec^2\phi \, d\phi + \frac{1}{R'_w} \int_0^{R'_w \sec\theta} \frac{J'(\hat{r}', t')}{\rho} \, d\hat{r}'}{\frac{R'_w}{N(\theta)} \int_0^{\theta} K(\phi, \theta) \sec^2\phi \, d\phi + \frac{2R'_w}{N(\theta)} \int_0^{\theta} k(\phi, \theta) \sin\phi \sec^3\phi \, d\phi - \frac{R'_w \sec^2\theta(t')}{2}}. \tag{IX.20}$$

References

[1] Ajaev, V. S. (2005). Spreading of thin volatile liquid droplets on uniformly heated surfaces. *Journal of Fluid Mechanics*, 528, 279-296.

[2] Blossey, R., & Bosio, A. (2002). Contact line deposits on cDNA microarrays: a "twin-spot" effect. *Langmuir*, 18(7), 2952-2954.

[3] Bromberg, V., Ma, S., & Singler, T. J. (2013). High-resolution inkjet printing of electrically conducting lines of silver nanoparticles by edge-enhanced twin-line deposition. *Applied Physics Letters*, 102(21), 214101.

[4] Burkhart, C.T. (2016) Characterizing the Transient Profile Shapes and Deposition Patterns of Desiccating Colloidal Droplets. *Thesis. Rochester Institute of Technology*, Accessed from http://scholarworks.rit.edu/theses/9213.

[5] Burkhart, C.T., Maki, K.L., Schertzer, M.J. (2016) Observation of Contact Line Dynamics in Evaporating Droplets Under the Influence of Electric Fields. *ASME. International Conference on Nanochannels, Microchannels, and Minichannels, ASME 2016 14th International Conference on Nanochannels, Microchannels, and Minichannels, Washington, DC*.

[6] Burkhart, C.T., Maki, K.L., Schertzer, M.J. (2016) Impact of Particle Selection on Nanoparticle Self-Assembly in Evaporating Colloidal Droplets. *ASME. ASME International Mechanical Engineering Congress and Exposition, Volume 7: Fluids Engineering*.

[7] Cussler, E. L. (2009). Diffusion: mass transfer in fluid systems. *Cambridge University Press.*

[8] Deegan R. D., Bakajin O., Dupont T. F., Huber G., Nagel S. R., & Witten T. A. (1997). Capillary flow as the cause of ring stains from dried liquid drops. *Nature*, 389(6653), 827.

[9] Deegan R. D., Bakajin O., Dupont T. F., Huber G., Nagel S. R., & Witten T. A. (2000). Contact line deposits in an evaporating drop. *Physical Review E*, 62(1), 756.

[10] de Gans, B. J., Duineveld, P. C., & Schubert, U. S. (2004). Inkjet printing of polymers: state of the art and future developments. *Advanced materials*, 16(3), 203-213.

[11] Dugas, V., Broutin, J., & Souteyrand, E. (2005). Droplet evaporation study applied to DNA chip manufacturing. *Langmuir*, 21(20), 9130-9136.

[12] Eral, H. B., Augustine, D. M., Duits, M. H., & Mugele, F. (2011). Suppressing the coffee stain effect: how to control colloidal self-assembly in evaporating drops using electrowetting. *Soft Matter*, 7(10), 4954-4958.

[13] Gelderblom H., Bloemen O. & Snoeijer J. H. (2012). Stokes flow near the contact line of an evaporating drop. *Journal of Fluid Mechanics*, 709, 69-84.

[14] Hu, H. & Larson, R. G. (2002). Evaporation of a sessile droplet on a substrate. *The Journal of Physical Chemistry B*, 106(6), 1334-1344.

[15] Hu, H. & Larson, R. G. (2005). Analysis of the microfluidic flow in an evaporating sessile droplet. *Langmuir*, 21(9), 3963-3971.

[16] Hu, H. & Larson, R. G. (2006). Marangoni effect reverses coffee-ring depositions. *The Journal of Physical Chemistry B*, 110(14), 7090-7094.

[17] Huh C. & Scriven L. E. (1971). Hydrodynamic model of steady movement of a solid/liquid/fluid contact line. *Journal of Colloid and Interface Science*, 35(1), 85-101.

[18] Jones, T. B. (2002). On the relationship of dielectrophoresis and electrowetting. *Langmuir*, 18(11), 4437-4443.

[19] Kang, K. H. (2002). How electrostatic fields change contact angle in electrowetting. *Langmuir*, 18(26), 10318-10322.

[20] Larson, R. G. (2014). Transport and deposition patterns in drying sessile droplets. *AIChE Journal*, 60(5), 1538-1571.

[21] Maki K. L. & Kumar S. (2011). Fast evaporation of spreading droplets of colloidal suspensions. *Langmuir*, 27(18), 11347-11363.

[22] Masoud, H. & Felske, J.D. (2009). Analytical solution for Stokes flow inside an evaporating sessile drop: Spherical and cylindrical cap shapes. *Physics of Fluids*, 21(4), 042102.

[23] Moffatt H. K. (1964). Viscous and resistive eddies near a sharp corner. *Journal of Fluid Mechanics*, 18(1), 1-18.

[24] Nathan, A., Ahnood, A., Cole, M. T., Lee, S., Suzuki, Y., Hiralal, P., & Haque, S. (2012). Flexible electronics: the next ubiquitous platform. *Proceedings of the IEEE, 100(Special Centennial Issue)*, 1486-1517.

[25] Park, J., & Moon, J. (2006). Control of colloidal particle deposit patterns within picoliter droplets ejected by ink-jet printing. *Langmuir*, 22(8), 3506-3513.

[26] Parsa, M., Harmand, S., & Sefiane, K. (2018). Mechanisms of pattern formation from dried sessile drops. *Advances in colloid and interface science*, 254, 22-47

[27] Popov Y. O. (2005). Evaporative deposition patterns: Spatial dimensions of the deposit. *Physical Review E*, 71(3), 036313.

[28] Roache P. J. (2004). Building PDE codes to be verifiable and validatable. *Computing in Science & Engineering*, 6(5), 30-38.

[29] Shimoni, A., Azoubel, S., & Magdassi, S. (2014). Inkjet printing of flexible high-performance carbon nanotube transparent conductive films by "coffee ring effect". *Nanoscale*, 6(19), 11084-11089.

[30] Yin, Z., Huang, Y., Bu, N., Wang, X., & Xiong, Y. (2010). Inkjet printing for flexible electronics: Materials, processes and equipments. *Chinese Science Bulletin*, 55(30), 3383-3407.

[31] Yunker, P. J., Still, T., Lohr, M. A., & Yodh, A. G. (2011). Suppression of the coffee-ring effect by shape-dependent capillary interactions. *Nature*, 476(7360), 308.